

Identification of a Complete $160\mu\text{m}$ Flux-Limited Sample of Infrared Galaxies in the ISO Lockman Hole 1-deg² Deep Fields: Source Properties and Evidence for Strong Evolution in the FIR Luminosity Function for ULIRGs

B. A. Jacobs¹, D. B. Sanders¹, D. S. N. Rupke^{1,2}, H. Aussel³, D. T. Frayer^{4,5}, O. Ilbert^{1,6}, J. S. Kartaltepe^{1,7}, K. Kawara⁸, D.-C. Kim^{2,9,10}, E. Le Floch^{1,3}, T. Murayama¹¹, V. Smolčić^{12,13,14}, J. A. Surace¹⁵, Y. Taniguchi¹⁶, S. Veilleux², and M. S. Yun¹⁷

ABSTRACT

We have identified a complete, flux-limited, ($S_{160} > 120$ mJy), sample of $160\mu\text{m}$ -selected sources from *Spitzer* observations of the 1-deg² ISO Deep Field region in the

¹Institute for Astronomy, University of Hawaii, 2680 Woodlawn Drive, Honolulu, HI 96822, USA; bjacobs@ifa.hawaii.edu, sanders@ifa.hawaii.edu, drupke@ifa.hawaii.edu

²Department of Astronomy, University of Maryland, College Park, MD 20742, USA; veilleux@astro.umd.edu

³AIM, Saclay, Bat 709, Orme des merisiers, 91191 Gif-sur-Yvette, France; herve.aussel@cea.fr, emeric.lefloch@cea.fr

⁴NASA Herschel Science Center, California Institute of Technology, MS 100-22, Pasadena, CA 91125, USA

⁵National Radio Astronomy Observatory, P.O. Box 2, Green Bank, WV 24944, USA ; dfrayer@nrao.edu

⁶Laboratoire d' Astrophysique de Marseille, Marseille, France; olivier.ilbert@oamp.fr

⁷National Optical Astronomy Observatory, 950 N. Cherry Ave., Tucson, AZ, 85719, USA; jeyhan@noao.edu

⁸Department of Astronomy, Graduate School of Science, University of Tokyo, 7-3-1 Hongo, Bunkyo-ku, Tokyo 113-0033, Japan

⁹Department of Astronomy, University of Virginia, P.O. Box 400325, Charlottesville, VA 22904, USA; dk3wc@mail.astro.virginia.edu

¹⁰National Radio Astronomy Observatory, 520 Edgemont Road, Charlottesville, VA 22903, USA

¹¹Astronomical Institute, Graduate School of Science, Tohoku University, Aramaki, Aoba, Sendai 980-8578, Japan

¹²ESO ALMA COFUND Fellow, European Southern Observatory, Karl-Schwarzschild-Strasse 2, 85748 Garching b. Muenchen, Germany

¹³Argelander Institut for Astronomy, Auf dem Hügel 71, Bonn, 53121, Germany

¹⁴ California Institute of Technology, MC 249-17, 1200 East California Boulevard, Pasadena, CA 91125

¹⁵Spitzer Science Center, California Institute of Technology 220-06, Pasadena, CA 91125, USA; jason@ipac.caltech.edu

¹⁶Research Center for Space and Cosmic Evolution, Ehime University, 2-5 Bunkyo-cho, Matuyama, 790-8577, Japan; tani@cosmos.phys.sci.ehime-u.ac.jp

¹⁷Department of Astronomy, University of Massachusetts, 619 Lederle Graduate Research Center, Amherst, MA 01003, USA; myun@astro.umass.edu

Lockman Hole. Ground-based UV, optical and near-infrared (NIR) photometry and optical spectroscopy have been used to determine colors, redshifts and masses for the complete sample of 40 galaxies. Spitzer-IRAC+MIPS photometry, supplemented by ISOPHOT data at $90\mu\text{m}$ and $170\mu\text{m}$, has been used to calculate accurate total infrared luminosities, $L_{\text{IR}}(8 - 1000\mu\text{m})$, and to determine the IR luminosity function (LF) of luminous infrared galaxies (LIRGs). The maximum observed redshift is $z \sim 0.80$ and the maximum total infrared luminosity is $\log(L_{\text{IR}}/L_{\odot}) = 12.74$. Over the luminosity range $\log(L_{\text{IR}}/L_{\odot}) = 10 - 12$, the LF for LIRGs in the Lockman Hole Deep Field is similar to that found previously for local sources at similar infrared luminosities. The mean host galaxy mass, $\log(M/M_{\odot}) = 10.7$, and dominance of HII-region spectral types, is also similar to what has been found for local LIRGs, suggesting that intense starbursts likely power the bulk of the infrared luminosity for sources in this range of L_{IR} . However for the most luminous sources, $\log(L_{\text{IR}}/L_{\odot}) > 12.0$, we find evidence for strong evolution in the $\text{LF} \propto (1+z)^{6\pm 1}$, assuming pure number density evolution. These ultraluminous infrared galaxies (ULIRGs) have a larger mean host mass, $\log(M/M_{\odot}) = 11.0$, and exhibit disturbed morphologies consistent with strong-interactions/mergers, and they are also more likely to be characterized by starburst-AGN composite or AGN spectral types.

Subject headings: galaxies: evolution, infrared: galaxies

1. Introduction

Deep surveys at rest-frame far-infrared (FIR) wavelengths are important for identifying statistically complete samples of luminous infrared galaxies (LIRGs: $L_{\text{IR}}/L_{\odot} > 11.0$) – objects that appear to produce the bulk of the bolometric infrared luminosity density in the universe, and which are often “hidden” and misidentified in deep UV-optical surveys. Until recently, progress has been relatively slow in identifying complete samples of FIR sources selected at wavelengths $\lambda = 100 - 200\mu\text{m}$, which corresponds to the wavelength range where the majority of LIRGs at $z < 1$ emit their peak emission. The *Infrared Astronomical Satellite (IRAS)* all-sky survey provided the first complete census of $60\mu\text{m}$ -selected galaxies in the local universe (e.g. Soifer et al. 1989; Sanders et al. 2003), but lacked the sensitivity and long wavelength coverage to detect LIRGs at $z > 0.05$. The *Infrared Space Observatory (ISO)* provided increased sensitivity and longer wavelength coverage, but background instabilities often limited the determination of exact source positions. The *Spitzer Space Telescope* eventually provided the combination of long wavelength sensitivity and background stability needed to detect sources at the $\sim 100\text{mJy}$ level with relatively accurate positions, and extensive follow-up observations are now underway to identify source properties and redshifts.

In this paper, we report observations first begun as part of the U.S-Japan ISO-ISOPHOT

Deep Survey of a $\sim 1\text{-deg}^2$ region in the Lockman Hole (Kawara et al. 1998; Oyabu et al. 2005), and later expanded to include more recent infrared observations of the same region obtained as part of the Spitzer Wide-area InfraRed Extragalactic (SWIRE) survey (Lonsdale et al. 2003). Our final sample consists of MIPS-160 μm sources with fluxes greater than 120mJy. Multi-wavelength follow-up observations include Keck spectra of the majority of the sources, along with UV-optical photometry from the Sloan Digital Sky Survey (SDSS: York et al. 2000) for all of our sources, NIR photometry from the 2-Micron All Sky Survey (2MASS: Skrutskie et al. 2006) for most of our sources, and VLA 1.4GHz continuum images of the ISO-ISOPHOT deep fields (Yun et al. 2003). While other surveys (e.g. COSMOS: Scoville et al. 2007) may offer superior (particularly ancillary) data, the Lockman Hole survey discussed here subtends a total of 1.2 deg^2 and is thus comparable in total area to similar existing datasets. This survey therefore substantially increases the total area to date at these wavelengths and helps guard against cosmic variance.

Sections 2 and 3 describe our field selection and identification of SWIRE MIPS-160 sources, respectively. Methods used for identifying optical counterparts are presented in § 3, along with UV-NIR photometry and optical spectroscopy for individual sources. The spectral energy distributions (SEDs) and calculated infrared luminosities (L_{IR}) for each source are presented in § 5, and these data are then used to determine the Infrared galaxy Luminosity Function (LF). Section 6 presents evidence for evolution in the LF at the highest infrared luminosities, as well as a discussion of the properties of the host galaxies, including morphology, colors, masses and spectral types. Our conclusions are presented in § 7.

2. Field Selection and FIR Observations

The Lockman Hole (LH) is a region of the sky with the smallest HI column density (Lockman et al. 1986) and thus has been a favorite target for deep extragalactic surveys, particularly in the FIR where confusion noise from infrared cirrus is expected to be at a minimum.

The LH was originally targeted for deep FIR observations with the *Infrared Space Observatory* (ISO) as part of the Japan/University of Hawaii (UH) ISO cosmology program that carried out observations of 2 small regions (LHEX and LHNW) using the ISOPHOT detector at 90 μm and 170 μm . Both LHEX and LHNW are $\sim 44' \times 44'$ in size (see Figure 1) - the former is centered at $\alpha = 10^{\text{h}}52^{\text{m}}00^{\text{s}}$, $\delta = 57^{\circ}00'00''$ and corresponds approximately to the field center of the *ROSAT* X-Ray Deep Survey Field (Hasinger et al. 1998), while the latter is centered at $\alpha = 10^{\text{h}}33^{\text{m}}55^{\text{s}}$, $\delta = 57^{\circ}46'20''$ and was chosen by the Japan/UH team to be centered on the true minimum HI column density position within the larger LH field. Note that a small sky area in the LHNW field was also mapped at 7 μm using ISOCAM on ISO (Taniguchi et al. 1997)

There is a fairly extensive published analysis of the ISOPHOT 90 μm and 170 μm data for

both LHEX and LHNW, including initial source counts (Kawara et al. 1998), and final source lists (Kawara et al. 2004), along with attempts to identify radio and near-infrared counterparts for individual sources (Yun et al. 2001; Sanders et al. 2001; Yun et al. 2003), and to obtain follow-up spectroscopy (Sanders et al. 2001; Oyabu et al. 2005). However, several factors prohibited using the ISOPHOT data for producing a well identified complete sample of FIR sources, first of which being the relatively large fluctuations in the ISOPHOT background, and the corresponding uncertainty in extracted source positions at both $90\mu\text{m}$ and $170\mu\text{m}$. Further complications came with the realization that several radio and NIR sources were often found within the relatively large FIR beam.

A major improvement in our ability to determine more reliable FIR fluxes and more accurate source positions was made possible once data from *Spitzer* were made public. In particular, SWIRE, a *Spitzer* Key Project (Lonsdale et al. 2003) included the LH as one of its deep survey areas¹. SWIRE obtained maps in all 7 *Spitzer* IRAC+MIPS bands (3.6, 4.6, 5.8, 8.0, 24, 70, $160\mu\text{m}$), and covered both LHEX and LHNW, except for a small portion of the LHNW region missed by IRAC as shown in Figure 1.

In this paper we use the SWIRE IRAC+MIPS data to produce a new flux-limited sample of FIR sources in the LHEX + LHNW fields. We also make use of all of our previous multi-wavelength imaging and spectroscopy along with new data from SDSS and 2MASS in order to first identify reliable optical counterparts, and then to determine redshifts and total infrared luminosities for each source. We also use these data to characterize host galaxy properties (e.g. masses, morphologies, spectral types) in order to better understand the nature of the infrared galaxy population.

3. The Lockman Hole $160\mu\text{m}$ Sample

The MIPS- $160\mu\text{m}$ detector samples emission at wavelengths closest to the rest-frame peak of the FIR/submillimeter SED of infrared luminous galaxies. Most galaxies detected at $160\mu\text{m}$ are also detected at MIPS- $70\mu\text{m}$ and MIPS- $24\mu\text{m}$ as well as all four IRAC bands. For these reasons, as was the case with previous ISO observations of the LHEX and LHNW fields, we continue to focus on selecting a complete sample of extragalactic sources at the longest observed FIR wavelength.

Figure 2 (left panel) shows the distribution of flux density of all ~ 500 sources in the SWIRE LH $160\mu\text{m}$ catalog. It is from this distribution that we take 120mJy as the flux limit for the sample. There are 39 SWIRE $160\mu\text{m}$ sources within the LHEX and LHNW fields down to a flux limit of 120mJy. The integral number counts from the catalog (Figure 2, right panel) follow a constant

¹The SWIRE data release paper is available at:
http://swire.ipac.caltech.edu/swire/astromers/publications/SWIRE2_doc_083105.pdf

slope at fluxes above the 120 mJy selection limit, and we therefore take the sample to be complete above this limit (e.g. Beichman et al. 1988; Soifer et al. 1989).

We also compared the MIPS-160 μ m catalog with our previous ISOPHOT 170 μ m catalog, and secondarily with the ISOPHOT 90 μ m catalog, and confirmed our previous suspicions that a significant fraction of the ISOPHOT 170 μ m sources were either spurious 3σ noise peaks or weaker sources with boosted flux due to non-Gaussian noise fluctuations. However, we also discovered a few sources where our previous ISOPHOT data along with MIPS-70 μ m data suggested that there should have been a MIPS-160 μ m source above 120mJy, yet there was no source listed in the MIPS-160 μ m catalog. For these cases we went directly to the MIPS images and found that in each case there was a source in the 160 μ m image, so we extracted our own flux at 160 μ m by performing point-spread function (PSF) fitting on the image. This was done in consultation with the SWIRE team so that our flux extraction method would be in agreement with that used to construct the SWIRE catalog. In all but one case our extracted MIPS-160 μ m flux fell below the 120mJy completeness limit. However, for J105252.76+570753.7, the extracted MIPS-160 μ m flux of 149mJy was above the completeness limit, thus this source was added to the final list, bringing the total number of sources to 40. The distribution of these 40 sources across the LHNW and LHEX fields is shown in Figure 3.

In addition, there are six sources listed in Table 1 that were included in the SWIRE MIPS-160 μ m catalog but not the MIPS-70 μ m catalog. This was somewhat surprising given the sensitivity of the MIPS-70 μ m catalog, and the expected 70 μ m flux assuming even a fairly extreme 160/70 flux ratio. All six sources were in fact visible in the 70 μ m image, and hence, we again performed PSF fitting in consultation with the SWIRE team to extract a 70 μ m flux. Thus all 40 of our MIPS-160 μ m sources now have measured MIPS-70 μ m fluxes.

4. Multiwavelength Data

4.1. UV/Optical and NIR Images

UV/optical and NIR imaging data are critical for identifying the sources responsible for the observed FIR emission, measuring redshifts and computing luminosities. The SWIRE data release actually includes optical ($g'r'i'$) images obtained at Kitt Peak National Observatory (KPNO) covering a large fraction of the LH field, with extracted photometry for those sources matched to the identified IRAC counterparts of MIPS-24 μ m sources (see below). However, SWIRE optical coverage is uneven across our fields, a central portion of the LHEX (ROSAT) field was not targeted for followup and the southwest portion of the LHNW field falls beyond the edge of the IRAC survey (see Figure 1) and consequently was also not observed in optical. As a result, almost half (19/40) of our MIPS-160 μ m sources lack KPNO $g'r'i'$ photometry in the SWIRE catalog. Fortunately, the

SDSS provides full coverage of the LH field, and we therefore make use of the *ugriz* catalog photometry from Data Release 7 as well as display color-composite images for all of the MIPS-160 μ m sources. Additionally we use 2MASS catalogs to obtain *JHK_s* photometry for the majority (27/40) of our MIPS-160 μ m sources.

4.2. Identification of Counterparts

As an initial step the 160 μ m sources were matched with their counterparts in the SWIRE 70 μ m, and IRAC+24 μ m+Optical catalogs. A series of image cutouts from each of the Spitzer IRAC+MIPS bands plus optical images from KPNO were then assembled for each source in order to identify the correct optical counterpart (see Figure 4 for an example²). The red, blue, and green circles overlaid on these images indicate the position of the centroid of each detection in the 160 μ m, 70 μ m, and bandmerged IRAC+24 μ m catalogs, respectively. Each 160 μ m source has one and only one counterpart in the 70 μ m images, and nearly all (36/40) have only one counterpart at 24 μ m. In the cases with multiple 24 μ m sources, we choose the source nearest the 160 μ m centroid. Table 1 lists the source identification numbers from the SWIRE catalogs, as well as coordinates of each source taken from the SWIRE IRAC+24 μ m+Optical catalog, except for sources lacking coverage in two or more IRAC bands (noted in the table) where we list coordinates from the SWIRE 24 μ m catalog. Following the identification of the Optical/IRAC counterpart for each of the MIPS-160 μ m sources, we then match these with objects in the 2MASS and SDSS catalogs and list their source IDs. In the case of 2MASS we prefer to quote the Extended Source Catalog (XSC) when a match is available, but also make use of the Point Source Catalog (PSC). The last two columns in Table 1 list the IDs assigned to sources by Oyabu et al. (2005) using observations from ISO. Table 2 lists the fluxes reported in the SWIRE, 2MASS, and SDSS catalogs along with our own flux measurements as described above.

4.3. Optical spectra

We collected spectroscopic data on the optical counterparts to the ISO sources from several sources, first of which was our library of Keck spectra obtained as part of the original ISO follow-up program which had targeted expected counterparts to the ISOPHOT 170 μ m sources. Both low- and moderate-resolution spectra were taken with the Echellette Spectrograph and Imager (ESI: Sheinis et al. 2000) over several observing runs: 2000 Mar 30 – 31 and 2001 Jan 23 – 24 UT for the low-resolution data; and 2001 Feb 27 – 28, 2002 Jan 16 – 17, 2002 Feb 16, and 2002 Mar 15 for the moderate-resolution data. The low-resolution spectra had previously been used for redshift identification of putative ISOPHOT 170 μ m counterparts and some of these data were published in

²Images of the complete sample are available at: <http://ifa.hawaii.edu/~bjacobs/LHonlinefigs.pdf>

Oyabu et al. (2005). The follow-up high-resolution spectra were obtained in order to make accurate emission-line flux measurements. These are published here for the first time. In total, we have Keck spectra for 19/40 (48%) of our complete sample. An example of our high-resolution Keck spectra is shown in Figure 5. In addition to Keck, we supplemented our redshift and flux measurements with public SDSS spectra (Adelman-McCarthy et al. 2007) for an additional 9 of our targets. All 28 of the Keck + SDSS spectra are published on-line in Figures 5.1-5.28³. In addition we list spectroscopic redshifts for 2 sources for which the spectra themselves are unavailable (see Table 3).

Ten of our MIPS-160 μ m sources do not have optical spectra. Most of these sources were either not properly identified in the earlier ISOPHOT-170 μ m images, or had several radio and K-band counterparts within the ISOPHOT-170 μ m beam where the dominant counterpart that had previously been targeted with Keck turned out not to be the correct source. For these 10 sources, we have been able to determine fairly accurate photometric redshifts, as described below.

4.4. VLA 1.4 GHz Radio Data

Deep 1.4 GHz radio continuum images of the LHEX and LHNW fields were obtained using the NRAO VLA in the B-configuration in February 2000 and March-April 2001 as part of the AY110 and AY121 programs. The angular resolution of the data are $\sim 5''$. The achieved sensitivity of the LHEX data is $1\sigma \sim 15 \mu\text{Jy}$ while the sensitivity for the LHNW field is a factor of 2 worse because of a bright (4.2 Jy) continuum source nearby. The photometry is done using the AIPS task SAD, which fits a 2D Gaussian to the brightness distribution, and total integrated flux is reported for extended sources in Table 2. A more detailed discussion of the radio data is presented by Oyabu et al. (2005).

5. Results

The complete photometric data set for each of our 40 MIPS-170 μ m sources is presented in Table 2. We use these data, along with the measured (spectroscopic) and computed (photometric) redshifts listed in Table 3, to construct SEDs for each source and to compute total infrared luminosities, which are then used to construct the luminosity function for our complete sample.

5.1. Photometric Redshifts

The majority of the SWIRE 160 μ m detections have spectroscopic data, which were used to determine their redshifts. For the 10 objects without spectra (noted with “Phot-z” in Table 3),

³See: <http://ifa.hawaii.edu/~bjacobs/LHonlinefigs.pdf>

we calculate a photometric redshift using the photometry from SDSS *ugriz*-bands (except for J103341.28+580221.4, see Table 3), 2MASS *JHK_s*-bands and IRAC 3.6 and 4.5 μm . A χ^2 template-fitting method (*Le Phare*) was used following the prescription given in Ilbert et al. (2009). This method offers an improvement in photo-*z* accuracy over previous methods, due primarily to improved calibration using large spectroscopic samples from VLT-VIMOS and Keck-DEIMOS. The best fit redshift values and uncertainties are listed in Table 3.

5.2. Spectral Energy Distributions and Infrared Luminosity

The photometry and redshifts were used to construct SEDs (νL_ν) for each source, which are shown in Figure 6 sorted in order of decreasing luminosity. The SEDs are characteristic of what has previously been observed for infrared-selected galaxies, with the most luminous sources showing a dominant “infrared bump” presumably due to thermal dust emission, and an “optical bump” due to thermal emission from stars. Although the mid-infrared sampling is relatively sparse, it is also possible to see the effects of emission from polycyclic aromatic hydrocarbons (PAHs) in the mid-infrared at $\lambda_{\text{rest}} \sim 4 - 12\mu\text{m}$, and silicate absorption at $\lambda_{\text{rest}} \sim 10\mu\text{m}$.

The SEDs displayed in Figure 6 also show template fits to the data. The MIPS and 8 μm points are fit to a library of SED templates by Siebenmorgen & Krugel (2007), and the best fit is shown as solid line. The dotted line in Figure 6 represents a stellar evolution model fit to the UV-NIR data which is used to estimate stellar masses (see below). To estimate each source’s total IR luminosity, $L_{\text{IR}}(8 - 1000\mu\text{m})$, we use the prescription described by Siebenmorgen & Krugel (2007). The use of this model of SED fitting to estimate IR luminosity over others, such as Chary & Elbaz (2001) or Dale & Helou (2002), is advocated by Symeonidis et al. (2008) largely due to the tendency of these models to underestimate the peak of the FIR luminosity as represented by the 160 μm flux. This tendency of Siebenmorgen & Krugel (2007) to better fit the FIR data held true for our 160 μm sample as well. Table 3 lists the computed infrared luminosity for each source.

5.3. Infrared Galaxy Luminosity Function

In addition to infrared luminosity, we use each source’s flux at 160 μm , and redshift ($H_0 = 75 \text{ km s}^{-1} \text{ Mpc}^{-1}$, $\Omega_{\text{m}} = 0.3$ and $\Omega_{\Lambda} = 0.7$ to calculate luminosity distance) to calculate a LF from our sample. Figure 7 shows the infrared LF resulting from our observations of the LH in comparison with the LF in the local Universe, previously determined from the IRAS Revised Bright Galaxy Sample (RBGS) all-sky survey, which has median and maximum redshifts: $z = 0.008$ and $z = 0.09$ (Sanders et al. 2003). The LF density values and uncertainties plotted in Figure 7 are listed in Table 4. We divide the data into bins of $\log(L_{\text{IR}}/L_{\odot}) = 0.4$ in size, corresponding to steps of one in absolute magnitude. Note that SWIRE detected galaxies, J103258.0+573105 and J105349.60+570708.1 at 160 μm , but we do not include them in our analysis because their calculated

total infrared luminosities are $\log(L_{\text{IR}}/L_{\odot}) = 9.55$ and 8.81 which results in them falling as the lone galaxy in their respective luminosity bins. The volume at which the survey is sensitive to galaxies below this luminosity range is small, so we restrict our attention to higher luminosity sources.

In comparing the LF of our LH data with the RBGS we are comparing a narrow deep survey with 40 galaxies to a wide local survey with several hundred galaxies. This means that the relative significance of each galaxy is higher for the LH, so it is important to have accurate luminosity estimates. On the other hand, the one-magnitude bins have the effect of mitigating uncertainties in luminosity, since they can include galaxies with luminosity estimates differing by as much as a factor of 2.5. This is particularly significant for the objects in the sample that have luminosity estimates using photometric redshifts, since their luminosity is less certain than the rest of the sample. The photometric redshifts and their 68% uncertainty limits are noted in Table 3, and these limits are used to estimate uncertainties in their luminosities. In addition to photometric redshift uncertainties, the errors in matching νL_{ν} to a model infrared luminosity become less important when the data are binned as described. The space density of galaxies within each bin is calculated using the method developed by Schmidt (1968), which accounts for the fact that in a flux-limited sample a larger range of luminosities is observable at small distances than at greater distances. He proposes using a measure of the volume that a particular flux measurement samples, given the flux limits of the survey. For example, a galaxy at redshift $z = 0.5$ with a flux at $160\mu\text{m}$ of 170mJy could have been seen at greater redshift (and hence represent a larger volume), since the flux limit of the sample is 120mJy . This volume sampling is characterized by the V/V_{max} parameter, where V is the volume corresponding to the redshift actually observed, and V_{max} is the maximum volume over which it could be observed. A mean V/V_{max} value of 0.5 within a luminosity bin indicates an even distribution of galaxies within the total volume sampled in that bin.

6. Discussion

6.1. Evidence For Possible Evolution in the Luminosity Function

The space density of galaxies with infrared luminosity ($8 - 1000\mu\text{m}$) in the range $\log(L_{\text{IR}}/L_{\odot}) = 10 - 12$ appears to be consistent between the RBGS and our LH sample. In particular, Sanders et al. (2003) fit a broken power-law to the RBGS sample. At $\log(L_{\text{IR}}/L_{\odot}) = 9.5 - 10.5$ the RBGS is fit with $\Phi(L) \propto L^{-0.6 \pm 0.1}$, and at $\log(L_{\text{IR}}/L_{\odot}) = 10.5 - 12.5$ the power-law is: $\Phi(L) \propto L^{-2.2 \pm 0.1}$. The Lockman Hole data for luminosities $\log(L_{\text{IR}}/L_{\odot}) < 12$, agree within their errors to these power-laws. This concurrence is to be expected given the relatively low redshifts sampled in these lower luminosity bins. At $\log(L_{\text{IR}}/L_{\odot}) > 12.0$ the situation changes. The co-moving space density of ultraluminous infrared galaxies (ULIRGs: $\log(L_{\text{IR}}/L_{\odot}) > 12.0$) in the $\log(L_{\text{IR}}/L_{\odot}) = 12.0 - 12.4$ luminosity bin is $\sim 7\times$ higher in the LH than in the RBGS. The median redshift of the ULIRGs in

the LH in this luminosity bin is $z = 0.51$. In the highest luminosity bin, $\log(L_{\text{IR}}/L_{\odot}) = 12.4 - 12.8$, the median redshift of the 4 LH galaxies in this bin is $z = 0.71$. To compare the co-moving space density with the RGBS in this bin we extrapolate the RGBS power-law to $\log(L_{\text{IR}}/L_{\odot}) = 12.6$ and find that the density in the LH sample is $\sim 11\times$ higher.

Our new results for the LF of the most luminous infrared galaxies in the LH are consistent with strong evolution in the co-moving space density of ULIRGs. If we assume pure space-density evolution of the form $(1+z)^n$, our new results for the LH imply $n \sim 6 \pm 1$. This is similar to what was found in an earlier study of the infrared luminosity function of ULIRGs by Kim & Sanders (1998), where the co-moving space density of ULIRGs in the IRAS 1-Jy sample (mean $z \sim 0.15$), was found to be $\sim 2\times$ larger than the local space density of ULIRGs in the RGBS (mean $z \sim 0.05$), implying $n = 7.6 \pm 3.2$. Our new results are also consistent with a recent determination of the extragalactic $250\mu\text{m}$ luminosity function by Dye et al. (2010), which shows a “smooth increase” with redshift of a factor of $3.6\times$ in the co-moving space density of luminous infrared sources between $z = 0$ and $z = 0.2$, corresponding to $n = 7.1$.

Deeper far-infrared surveys currently underway with *Spitzer* and *Herschel* will eventually allow us to determine whether the strong evolution observed for the most luminous infrared extragalactic sources in the relatively nearby universe continues out to higher redshift. For now, we simply note that if we assume similar strong evolution, e.g. $(1+z)^6$, in the ULIRG population out to higher redshifts, our results would imply a co-moving space-density of ULIRGs that is $\sim 700\times$ larger at $z \sim 2$ compared to the value at $z = 0$. Is there evidence for such a large population of ULIRGs at high redshift? The answer seems to be yes. There is a population of faint submillimeter sources detected by the Submillimeter Common User Bolometer Array (SCUBA) on the James Clerk Maxwell Telescope (JCMT), which has been interpreted variously as exotic objects, or ULIRGs at high redshift (Smail et al. 1997; Hughes et al. 1998; Barger et al. 1998; Lilly et al. 1999). Lilly et al. argued that these objects are indeed ULIRGs at $z \sim 2$. Subsequently, Chapman et al. (2005) measured a range of spectroscopic redshifts, $z = 1.7 - 2.8$ for a sample of 73 submillimeter galaxies, and suggested an evolution in number density of three orders of magnitude for ULIRGs between $z = 0$ and $z \sim 2.5$. Our results for ULIRGs in the LH, when extrapolated out to $z = 2 - 2.5$ are then consistent with the hypothesis that the SCUBA submillimeter sources are indeed ULIRGs.

6.2. Galaxy Properties

To achieve a better understanding of the processes responsible for the observed infrared emission and the nature of the galaxies in our MIPS- $160\mu\text{m}$ sample, we use our UV-NIR imaging data and optical spectra to determine galaxy morphology and masses, and spectral types, respectively.

6.2.1. Imaging: Morphology and Masses

In order to develop a picture of the morphologies, and to gain an indication of the prevalence of merging/interacting galaxies in the sample we examine their UV-NIR images. We compile color composite images of the sources from those available through the Finding Chart section of the SDSS DR7 website, and show these in luminosity order in Figure 8. The zoom on these cutouts is scaled so that each box is 100kpc on a side. At high redshifts and thus high zoom, the image quality of the SDSS charts is low, so for sources with $z > 0.3$ we display stacked $g'r'i'$ images from KPNO when available. A brief description of the galaxy morphologies is presented in Table 5. Many of the higher luminosity sources with $\log(L_{\text{IR}}/L_{\odot}) > 11.5$ exhibit features suggestive of interactions/mergers, such as multiple cores and/or tidal tails. At luminosities lower than $\log(L_{\text{IR}}/L_{\odot}) < 11$ the large majority of sources appear to be mostly unperturbed spirals. These trends are consistent with previous studies of local samples of LIRGs and ULIRGs (e.g. Sanders & Mirabel 1996), which have shown that strong interactions and mergers appear responsible for triggering the most luminous infrared sources.

Stellar masses for each of the MIPS-160 μm sources are listed in Table 5. The masses were computed by fitting the UV-NIR SEDs using *Le Phare* (Ilbert et al. 2010) and assuming a Chabrier (Chabrier 2003) initial mass function (IMF). The mass range is $\log(M/M_{\odot}) \sim 10.0 - 11.5$ corresponding to $\sim 0.5 - 3M^*$. Higher mass systems are more likely to be associated with higher infrared luminosity.

6.2.2. Spectroscopy: Extinction, Abundances and Spectral Types

Our high-resolution Keck/ESI spectra, supplemented by SDSS spectra and four low-resolution ESI spectra, allow us to measure robust spectral types for 25 of the 160 μm sources in our sample. An example of these spectra was shown in Figure 5. Spectra for the 25 sources with spectral types as well as those from three sources for which we have data but were unable to measure spectral types are available in the online edition of the Journal. After carefully accounting for the effects of stellar absorption and applying an extinction correction (median $E(B - V) = 0.7$), we classify the spectra as H II-region-like, or star-forming (H); composite, or star formation + an AGN (C); Seyfert (S); or LINER (L), based on the classification scheme proposed by Kewley et al. (2006) (see Figure 9). Table 3 lists the measured spectral types and extinctions for each galaxy when they are available.

Dividing the subsample with spectral types into luminosity bins, we find that 15 of 19, (79%), of galaxies in the $\log(L_{\text{IR}}/L_{\odot}) < 11$ bin have H II-region-like spectral type, consistent with star formation as the dominant source of excitation. This is close to the H II-region-like fraction of nearby galaxies selected at 60 μm ($\sim 70\%$ – Veilleux et al. 1995; Yuan et al. 2010). The other four galaxies include one Seyfert and one LINER and 2 objects with mixed types that suggest a “composite” starburst-AGN mixture of excitation. Only six galaxies with high resolution spectroscopy

(and hence derived spectral types) have $\log(L_{\text{IR}}/L_{\odot}) > 11$. Three ($3/6 = 50\%$) have H II-region-like spectral type, one is a Seyfert, one is a Seyfert/LINER, and one is a “composite” mixture of starburst/LINER excitation. Although the fraction of galaxies with H II-region-like spectral types decreases at higher infrared luminosity (similar to what is observed for nearby galaxies selected at $60\mu\text{m}$), the number statistics in this high luminosity bin are too low to draw conclusions about the fractions of different spectral types. In an attempt to provide additional information on the spectral types of our high infrared luminosity sources, we have employed a new technique developed from studies of SDSS galaxies (Smolčić et al. 2008) that maps UV/optical continuum colors onto the spectral line diagnostic diagram. This method is described in the Appendix, where the SDSS photometry for all of our MIPS- $160\mu\text{m}$ sources is used to derive “P1,P2” photometric spectral types for each source, following the prescription given by Smolčić et al. (2008). These results both confirm the large H II-region-like fraction among the lower luminosity infrared sources, and show that composite and AGN spectral types appear to increase among the highest luminosity sources.

Because our spectra also contain the [O II] $\lambda\lambda 3727, 3729$ doublet, we are able to estimate gas-phase oxygen abundances for these systems. Where available, these are listed in Table 5, using the robust [N II]/[O II] diagnostic of Kewley et al. (2002). To put these in context, we also used the measured K_s data to compare to the luminosity-metallicity relation in the NIR (Salzer et al. 2005). For the 8 systems that have sufficient information (upper-branch R_{23} gas abundances and measured luminosities; see Rupke et al. (2008) for more on the methodology), we find that 5 follow the $L - Z$ relation of normal galaxies. Three others have higher luminosities than the data threshold, and appear to be slightly below the $L - Z$ relation (by $0.1 - 0.2$ dex), as found for other infrared-selected objects at high luminosity (Rupke et al. 2008).

6.2.3. Radio-FIR Correlation

The measured 1.4 GHz radio continuum fluxes are converted to 1.4 GHz radio power $L_{1.4\text{GHz}}$ assuming a spectral index of $\alpha = +0.75^4$, and they are plotted as a function of redshift on the left panel of Figure 10. The observed 1.4 GHz radio power range between 10^{20} and $10^{24.3}$ W Hz^{-1} (see Table 3), similar to the IR-selected galaxies in the local universe studied by Yun et al. (2001b), and none of the sources has sufficient radio power to be classified as a “radio-loud” object. The most luminous infrared sources also tend to be those with the largest radio luminosities, i.e. $\log(L_{1.4\text{GHz}}) = 23.0 - 24.4$, equivalent to the radio powers typically seen among Seyfert galaxies, and thus the presence of a low luminosity AGN cannot be ruled out based on these radio powers alone.

The well-known correlation between the measured infrared luminosity and radio power for star

⁴Spectral index α is defined as $S_{\nu} = S_0(\frac{\nu}{\nu_0})^{-\alpha}$.

forming galaxies is often quantified using the ratio commonly referred to as “ q -value”

$$q = \log [(FIR/3.75 \times 10^{12} \text{ Hz})/S_{1.4\text{GHz}}] \quad (1)$$

where FIR is the far-infrared flux density and $S_{1.4\text{GHz}}$ is in $\text{W m}^{-2} \text{ Hz}^{-1}$ (Condon 1992; Yun et al. 2001b). We computed these q -values using the $L_{1.4\text{GHz}}$ derived above and L_{FIR} computed from the best-fit SED models integrated between $\lambda = 40$ and $500 \mu\text{m}$, where the wavelength range has been chosen to match the original definition of L_{FIR} used to compute “ q ”. As shown on the right panel in Figure 10, the derived q -values of the LH 160 μm sources fall between 1.6 and 3.0, suggesting that most of these sources follow the same radio-FIR correlation as the local star forming galaxy populations. Some of the low redshift ($z \lesssim 0.15$) sources appear to have q -values on the high end of the local population. These are also the sources with the largest angular size, and the VLA measurements are likely under-estimates as a consequence. None of the LH 160 μm sources has a q -value less than 1.6 and thus a clear evidence for a radio-loud AGN.

7. Summary

We have made use of Spitzer-SWIRE imaging data of two $\sim 0.5\text{deg}^2$ fields (LHEX and LHNW) in the Lockman Hole, to identify a complete sample of 40 MIPS-160 μm selected extragalactic sources, with $S_{160} > 120\text{mJy}$. In combination with Keck spectroscopy and photometry from SDSS and 2MASS, we have obtained redshifts and infrared luminosities, and have attempted to characterize the host galaxy properties for all of the objects in the sample. The luminosity function for the MIPS-160 μm sample has been compared with the “local” ($z \leq 0.05$) luminosity function of FIR galaxies previously derived using the IRAS all-sky survey.

Our main results can be summarized as follows:

- (1) The complete $S_{160} > 120\text{mJy}$ sample contains 40 galaxies with infrared luminosities in the range $\log(L_{\text{IR}}/L_{\odot}) = 8.81 - 12.74$, with a maximum redshift: $z = 0.80$. The cumulative source counts down to 120mJy are estimated to be 1.2×10^5 sources sr^{-1} at 160 μm .
- (2) The luminosity function of the sources with $\log(L_{\text{IR}}/L_{\odot}) \sim 9.5 - 11.5$ is similar to that found previously for infrared galaxies in the IRAS 60 μm local galaxy sample.
- (3) The co-moving space density of the MIPS-160 μm galaxies with $\log(L_{\text{IR}}/L_{\odot}) > 12$ is $\sim 10\times$ higher than that for the local infrared galaxies with similar infrared luminosities found in the IRAS RBGS. Assuming pure number density evolution proportional to $(1+z)^n$, these results give $n = 6 \pm 1$, which implies strong evolution of the most luminous infrared sources, in contrast to little or no evolution observed in the number density of lower luminosity objects with $\log(L_{\text{IR}}/L_{\odot}) < 11$.
- (4) The host galaxy masses for our sample are in the range $\log(M_{\star}/M_{\odot}) \sim 10.0 - 11.5$ ($0.5 - 3M^*$), with evidence for an increase in host mass from a mean of 10.7 to 11.0 for objects with infrared luminosities below and above $\log(L_{\text{IR}}/L_{\odot}) = 11$, respectively.
- (5) The morphology and spectral types for our flux-limited sample of 160 μm -selected sources

generally agree with what has been observed locally for $60\mu\text{m}$ -selected samples. At $\log(L_{\text{IR}}/L_{\odot}) > 11$, the fraction of disturbed and/or merger systems and the fraction of objects with “composite” and/or AGN spectral types increases with increasing L_{IR} . At $\log(L_{\text{IR}}/L_{\odot}) < 11$ most objects appear to be either unperturbed spirals and/or weakly interacting systems with spectral types typical of HII regions.

(6) None of the LH sources has sufficient radio power to be classified as a “radio-loud” object. However, the most luminous infrared sources also tend to have the highest radio luminosities, i.e. $\log(L_{1.4\text{GHz}}) = 23.0 - 24.4$, equivalent to the radio powers typically seen among Seyfert galaxies, and thus the presence of a low luminosity AGN cannot be ruled out based on these radio powers alone.

8. Acknowledgments

We benefited from the published data and preliminary analyses of S. Oyabu. VS acknowledges support from the Owens Valley Radio Observatory, which is supported by the National Science Foundation through grant AST-0838260, and also received funding from the European Union’s Seventh Framework programme under grant agreement 229517. YT was financially supported in part by the Ministry of Education, Culture, Sports, Science and Technology (Nos. 10044052 and 10304013), and by the JSPS (Nos. 15340059, 17253001 and 19340046). This research has made use of the NASA/IPAC Extragalactic Database (NED) which is operated by the Jet Propulsion Laboratory, California Institute of Technology, under contract with the National Aeronautics and Space Administration. This publication makes use of data products from the Two Micron All Sky Survey, which is a joint project of the University of Massachusetts and the Infrared Processing and Analysis Center/California Institute of Technology, funded by the National Aeronautics and Space Administration and the National Science Foundation. Funding for the SDSS and SDSS-II has been provided by the Alfred P. Sloan Foundation, the Participating Institutions, the National Science Foundation, the U.S. Department of Energy, the National Aeronautics and Space Administration, the Japanese Monbukagakusho, the Max Planck Society, and the Higher Education Funding Council for England. The SDSS Web Site is <http://www.sdss.org/>.

The SDSS is managed by the Astrophysical Research Consortium for the Participating Institutions. The participating institutions are the American Museum of Natural History, Astrophysical Institute Potsdam, University of Basel, University of Cambridge, Case Western Reserve University, University of Chicago, Drexel University, Fermilab, the Institute for Advanced Study, the Japan Participation Group, Johns Hopkins University, the Joint Institute for Nuclear Astrophysics, the Kavli Institute for Particle Astrophysics and Cosmology, the Korean Scientist Group, the Chinese Academy of Sciences (LAMOST), Los Alamos National Laboratory, the Max-Planck-Institute for Astronomy (MPIA), the Max-Planck-Institute for Astrophysics (MPA), New Mexico State Univer-

sity, Ohio State University, University of Pittsburgh, University of Portsmouth, Princeton University, the United States Naval Observatory, and the University of Washington.

A. Using rest-frame colors to assign galaxy types

In an attempt to determine the spectral type of the 12 galaxies in our sample for which we lack optical spectra, we make use of a photometric (rest-frame color based) method extensively studied in Smolčić et al. (2008). Smolčić et al. (2006) have shown that principal component rest-frame colors (P1 and P2 hereafter) drawn from the modified Strömgren photometric system (3500–5800 Å; Odell et al. 2002) essentially trace the position of a galaxy in the BPT diagram (Baldwin, Phillips & Terlevich 1981; Kewley et al. 2001, 2006; Kauffmann et al. 2003). Hence, they can be used as efficient tracers of galaxy type, such as low-luminosity AGN (Seyfert and LINER), star forming, and composite galaxies (see Smolčić et al. 2006, 2008 for more details). Here we extend the method developed by Smolčić et al. (2008), that utilizes only the P1 color to disentangle star forming from AGN galaxies, to a probabilistic approach that uses both, P1 and P2 colors, and we adapt it to an IR- (rather than radio-) selected sample.

A.1. Derivation of P1, P2 colors

Given that we have SDSS *ugriz* photometry for the complete MIPS-160 μ m sample, we derive the P1 and P2 colors for all 40 galaxies in our sample by fitting their SEDs (encompassed by the SDSS *ugriz* photometry) with 100,000 spectra from the Bruzual & Charlot (2003) stellar population synthesis model library. Before performing the χ^2 minimization fit we redshift all the model spectra to the galaxy’s spectroscopic redshift. The colors are then computed from the best fit model spectrum (see Sec. 4.2. in Smolčić et al. 2008 for more details about the SED fitting).

To assess the accuracy of photometrically synthesized colors for IR-selected galaxies, we have derived the (P1,P2) colors via SED fitting (in the same way as described above) for an *IR-selected control sample* with available (P1,P2) colors computed independently from their spectra. The control sample, limited to a redshift range of 0.04 to 0.3, contains ~ 1350 galaxies drawn from the SDSS DR1 “main” spectroscopic galaxy sample matched to the IRAS Faint Source Catalog (see Obrić et al. 2006 for details about the cross-correlation of the catalogs). The spectroscopically derived (P1,P2) colors have been synthesized by Smolčić et al. (2006) by convolving the SDSS high-resolution spectra with the Strömgren filter system. They estimated that these spectroscopically derived rest-frame colors are accurate to 0.03 mag.

In Figure 11 we show the difference between the photometrically and spectroscopically derived (P1,P2) colors for our IR-selected control galaxies as a function of the photometrically derived P1 color. We use the median offset as a function of P1 to correct the photometrically derived colors, i.e. to scale these to the SDSS spectroscopic system. The distribution of the (P1,P2) color differences

after the corrections have been applied are shown in Figure 12. As expected, the corrections have eliminated systematic effects. Furthermore, as the accuracy of the spectroscopically derived colors has been shown to be 0.03 mag (Smolčić et al. 2006), the accuracy of the photometrically derived (P1,P2) colors is likely better than 0.12 and 0.03, respectively. It is remarkable that the accuracy of the P2 color derived via SED fitting is comparable to that of the spectroscopically derived color.

A.2. Classifying the Lockman galaxies using the P1-P2 color method

In Figure 13 we show the P1 vs. P2 the distribution for our 40 galaxies in our MIPS-160 μ m sample (their P1,P2 colors were corrected for systematic offsets as described in the previous section; filled dots). To assess the nature of these 40 galaxies for each one we compute the probability that it is a star forming, composite, AGN or absorption galaxy given its (P1,P2) rest-frame colors. The probability is computed based on the underlying distribution of our ~ 1300 control (SDSS-IRAS; $0.04 < z < 0.3$) galaxies (spectroscopically divided into absorption, star forming, AGN and composite galaxies using the standard diagnostics; Baldwin, Phillips & Terlevich 1981; Kewley et al. 2001; Kauffmann et al. 2003) in the P1-P2 plane as follows. We bin the P1-P2 plane in 2 dimensions. The size of the bins is taken to be about 2 times the photometric color uncertainty (see previous section). For each (P1,P2) bin we then calculate the probability as the ratio of the number of each (spectroscopically classified) galaxy type relative to the total number of control galaxies in that bin. Given the photometrically synthesized (P1,P2) colors for our Lockman galaxies we can then access the probability of each galaxy being a star forming, AGN, composite or absorption galaxy. These probability contours are shown in Figure 13, and our results are summarized in Table 6.

REFERENCES

- Adelman-McCarthy, J. K., et al. 2007, *ApJS*, 172, 634
- Baldwin, J. A., Phillips, M. M., & Terlevich, R. 1981, *PASP*, 93, 5
- Barger, A. J., Cowie, L. L., Sanders, D. B., Fulton, E., Taniguchi, Y., Sato, Y., Kawara, K., & Okuda, H. 1998, *Nature*, 394, 248
- Beichman, C. A., Neugebauer, G., Habing, H. J., Clegg, P. E., & Chester, T. J. 1988, *Infrared Astronomical Satellite (IRAS) Catalogs and Atlases, Vol. 1: Explanatory Supplement* (Washington, DC: GPO) 1
- Bruzual, G., & Charlot, S. 2003, *MNRAS*, 344, 1000
- Chabrier, G. 2003, *PASP*, 115, 763
- Chapman, S. C., Blain, A. W., Smail, I., Ivison, R. J. 2005, *ApJ*, 622, 772

- Chary, R. & Elbaz, D. 2001, *ApJ*, 556, 562
- Condon, J. J. 1992, *ARA&A*, 30, 575
- Dale, D. A. & Helou, G. 2002, *ApJ*, 576, 159
- Dye, S. et al. 2010, *A&A*, 518, L10
- Hasinger, G., Burg, R., Giacconi, R., Schmidt, M., Trumper, J., & Zamorani, G. 1998, *A&A*, 329, 482
- Hughes, D., et al. 1998, *Nature*, 394, 241
- Ilbert, O, et al. 2009, *ApJ*, 690, 1236
- Ilbert, O, et al. 2010, *ApJ*, 709, 644
- Kauffmann, G., et al. 2003, *MNRAS*, 341, 33
- Kawara, K., et al. 1998, *A&A*, 336, L9
- Kawara, K., et al. 2004, *A&A*, 413, 843
- Kewley, L. J., Dopita, M. A., Sutherland, R. S., Heisler, C. A., & Trevena, J. 2001, *ApJ*, 556, 121
- Kewley, L. J., & Dopita, M. A. 2002, *ApJS*, 142, 35
- Kewley, L. J., Groves, B., Kauffmann, G., & Heckman, T. 2006, *MNRAS*, 372, 961
- Kim, D.-C. & Sanders, D. B. 1998, *ApJS*, 119, 41
- Lilly, S. J., Eales, S. A., Gear, W. K. P., Hammer, F., Le Fevre, O., Crampton, D., Bond, J. R., & Dunne, L. 1998, *ApJ*, 518, 641
- Lockman, F. J., Jahoda, K. & McCammon, D. 1986, *ApJ*, 302, 432
- Lonsdale, C. J., et al. 2003, *PASP*, 115, 897
- Obrić, M., et al. 2006, *MNRAS*, 370, 1677
- Odell, A. P., Schombert, J., & Rakos, K. 2002, *AJ*, 124, 3061
- Oyabu, S., et al. 2005, *AJ*, 130, 2019
- Rupke, D. S. N., Veilleux, S., & Baker, A. J. 2008, *ApJ*, 674, 172
- Salzer, J. J., Lee, J. C., Melbourne, J., Hinz, J. L., Alonso-Herrero, A., & Jangren, A. 2005, *ApJ*, 624, 661
- Sanders, D. B., & Mirabel, I. F. 1996, *ARAA*, 34, 749

- Sanders, D. B., et al. 2001, in Springer Proc. Phys. 88, Starburst Galaxies: Near and Far, ed. L. Tacconi & D. Lutz (Heidelberg: Springer-Verlag) 297
- Sanders, D. B., Mazzarella, J. M., Kim, D.-C., Surace, J. A., & Soifer, B. T. 2003, AJ, 126, 1607 (RBGS)
- Schmidt, M. 1968, ApJ, 151, 393
- Sheinis, A. I., Miller, J. S., Bolte, M., & Sutin, B. M. 2000, Proc. SPIE, 4008, 522
- Scoville, N. Z., et al. 2007, ApJS, 172, 1
- Siebenmorgen, R., & Krugel, E. 2007, A&A, 461, 445
- Skrutskie, M. F. et al., 2006, AJ, 131, 1163
- Smail, I., Ivison, R. J., & Blain, A. W. 1997, ApJL, 490, L5
- Smolčić, V., et al. 2006, MNRAS, 371, 121
- Smolčić, V., et al. 2008, ApJS, 177, 14
- Soifer, B.T., Boehmer, L., Neugebauer, G., & Sanders, D.B. 1989, AJ, 98, 766 (BGS)
- Symeonidis, M., Willner, S. P., Rigopoulou, D., Huang, J.-S., Fazio, G. G., & Jarvis, M. J. 2008, MNRAS, 385, 1015
- Taniguchi, Y. et al. 1997, A&A, 328, L9
- Veilleux, S., Kim, D.-C., Sanders, D. B., Mazzarella, J. M., & Soifer, B. T. 1995, ApJS, 98, 171
- York, D. G., et al. 2000, AJ, 120, 1579
- Yuan, T., Kewley, L. J. & Sanders, D. B. 2010, ApJ, 709, 884
- Yun, M. S., Sanders, D., Kawara, K., Oyabu, S., Taniguchi, Y., & Okuda, H. 2001a, in ASP Conf. Proc. 240, Gas and Galaxy Evolution, ed. J. E. Hibbard, M. Rupen, & J. H. van Gorkom (San Francisco, CA: ASP), 123
- Yun, M. S., Reddy, N. A., & Condon, J. J. 2001b, ApJ, 554, 803
- Yun, M. S., Oyabu, S., Kawara, K., Okuda, H., Sanders, D., Veilleux, S., Murayama, T., & Taniguchi, Y. 2003, RMxAC, 17, 271

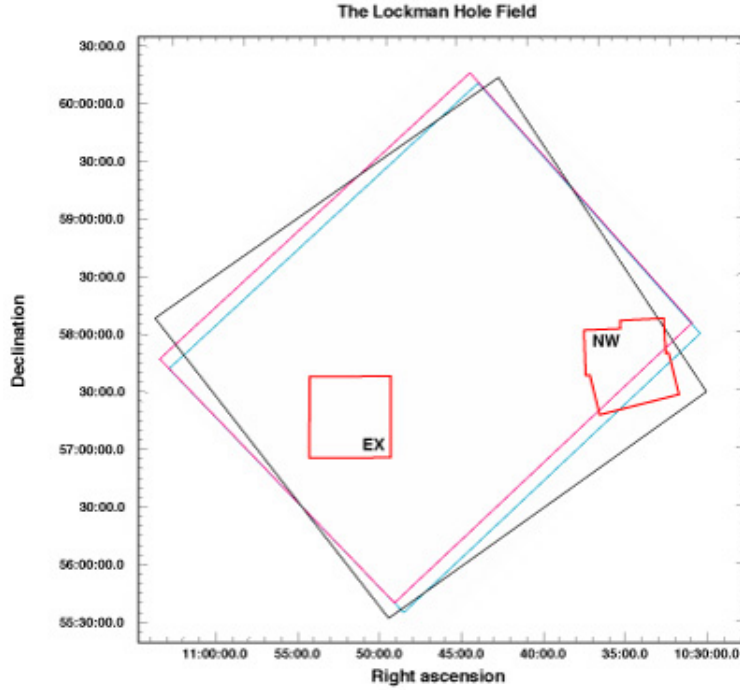


Fig. 1.— SWIRE and ISO coverage of the Lockman Hole. The black box denotes the area covered by SWIRE MIPS observations, the magenta box denotes the SWIRE IRAC channels 1 and 3, and the cyan box denotes SWIRE IRAC channels 2 and 4. The red square marks the location of observations of the ISO LHEX region, the red polygon towards the right of the image marks the ISO LHNW region.

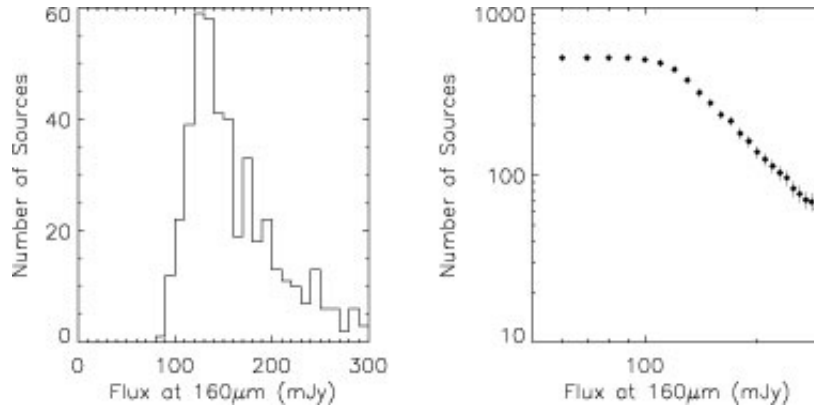


Fig. 2.— Left panel: Distribution of fluxes of the ~ 500 sources in the SWIRE LH $160\mu\text{m}$ catalog. Each bin is 10mJy wide. Right panel: Integral number counts versus flux of sources in the SWIRE LH $160\mu\text{m}$ catalog (horizontal axis ranges from 50 to 300 mJy). Vertical bars denote Poisson uncertainty.

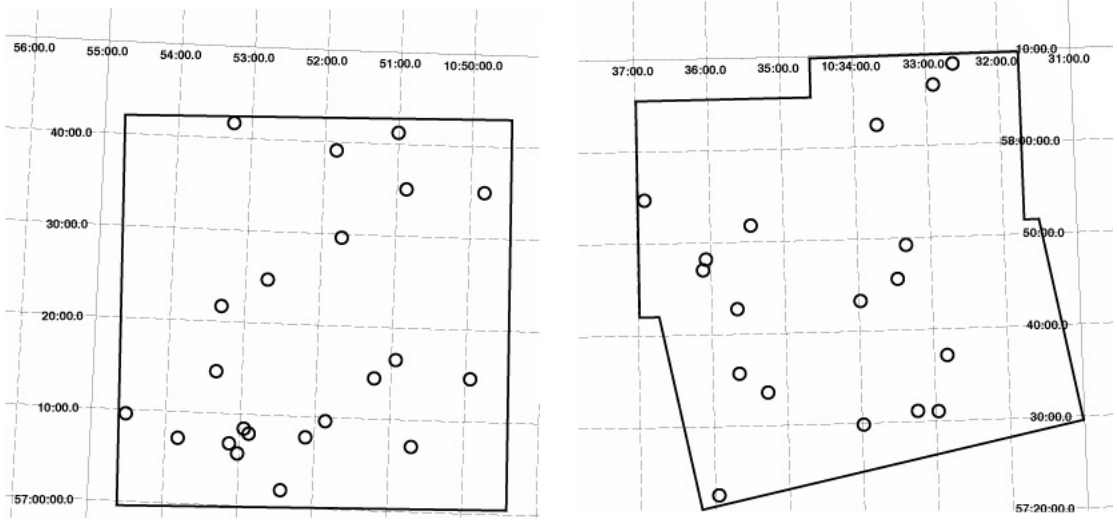


Fig. 3.— Left panel: LHEX subregion of the LH. The coverage of LHEX is roughly: $\alpha = 10^{\text{h}}49^{\text{m}}30^{\text{s}} - 10^{\text{h}}54^{\text{m}}30^{\text{s}}$ and $\delta = 57^{\circ}00'00'' - 57^{\circ}44'00''$. The circles denote the location of the $160\mu\text{m}$ sources. Right panel: LHNW subregion of the LH denoted by the large polygon. The coverage of LHNW is roughly: $\alpha = 10^{\text{h}}31^{\text{m}}00^{\text{s}} - 10^{\text{h}}37^{\text{m}}00^{\text{s}}$ and $\delta = 57^{\circ}20'00'' - 58^{\circ}10'00''$.

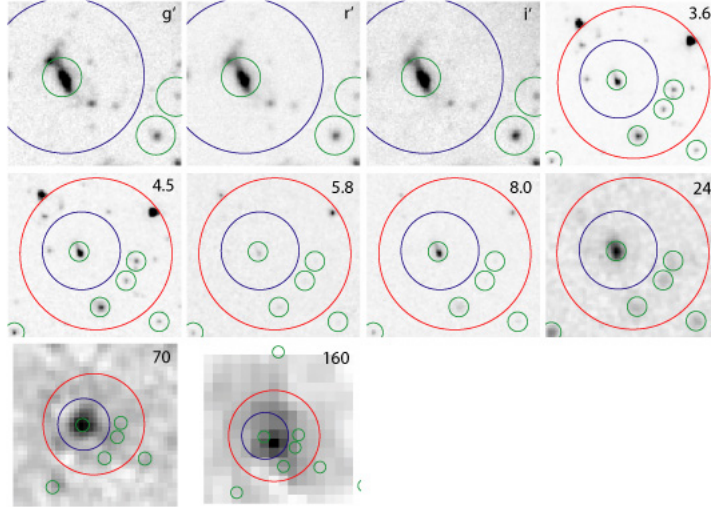


Fig. 4.— Images of source J103320.32+574913.6 at g' , r' , i' -bands, and 3.6, 4.5, 5.8, 8.0, 24, 70, $160\mu\text{m}$. The red, blue, and green circles indicate the position of the centroid of each detection in the $160\mu\text{m}$, $70\mu\text{m}$, and bandmerged IRAC+ $24\mu\text{m}$ catalogs, respectively. The radii of the circles are set to $40''$, $20''$, and $5''$ in all images (for all sources), and are meant to be rough indicators of the size of the PSF for the $160\mu\text{m}$, $70\mu\text{m}$, and $24\mu\text{m}$ sources. Figures 4.1 – 4.40 display cutout images for the entire sample of $160\mu\text{m}$ sources and are available at: <http://ifa.hawaii.edu/~bjacobs/LHonlinefigs.pdf>

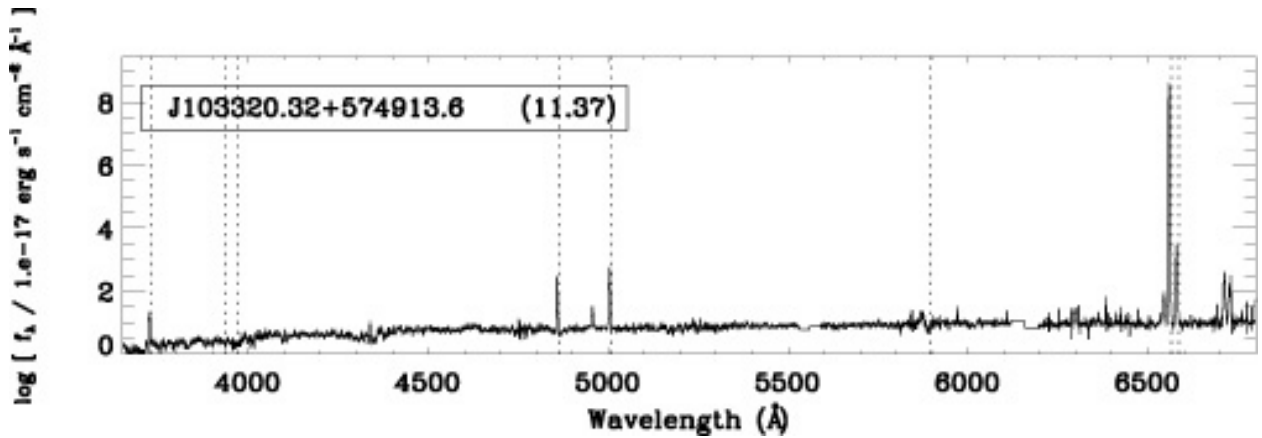


Fig. 5.— Example spectrum of J103320.32+574913.6 (see Table 3 for the source of the data). The wavelength range is $3650 - 6800\text{\AA}$, and the vertical lines mark the positions of [OII]3726/3729, CaII H & K, $H\beta$, [OIII]5007, NaI D, $H\alpha$, and [NII]6583. Figures 5.1– 5.28 display spectra for the 28 sources for which we have data, see: <http://ifa.hawaii.edu/~bjacobs/LHonlinefigs.pdf>

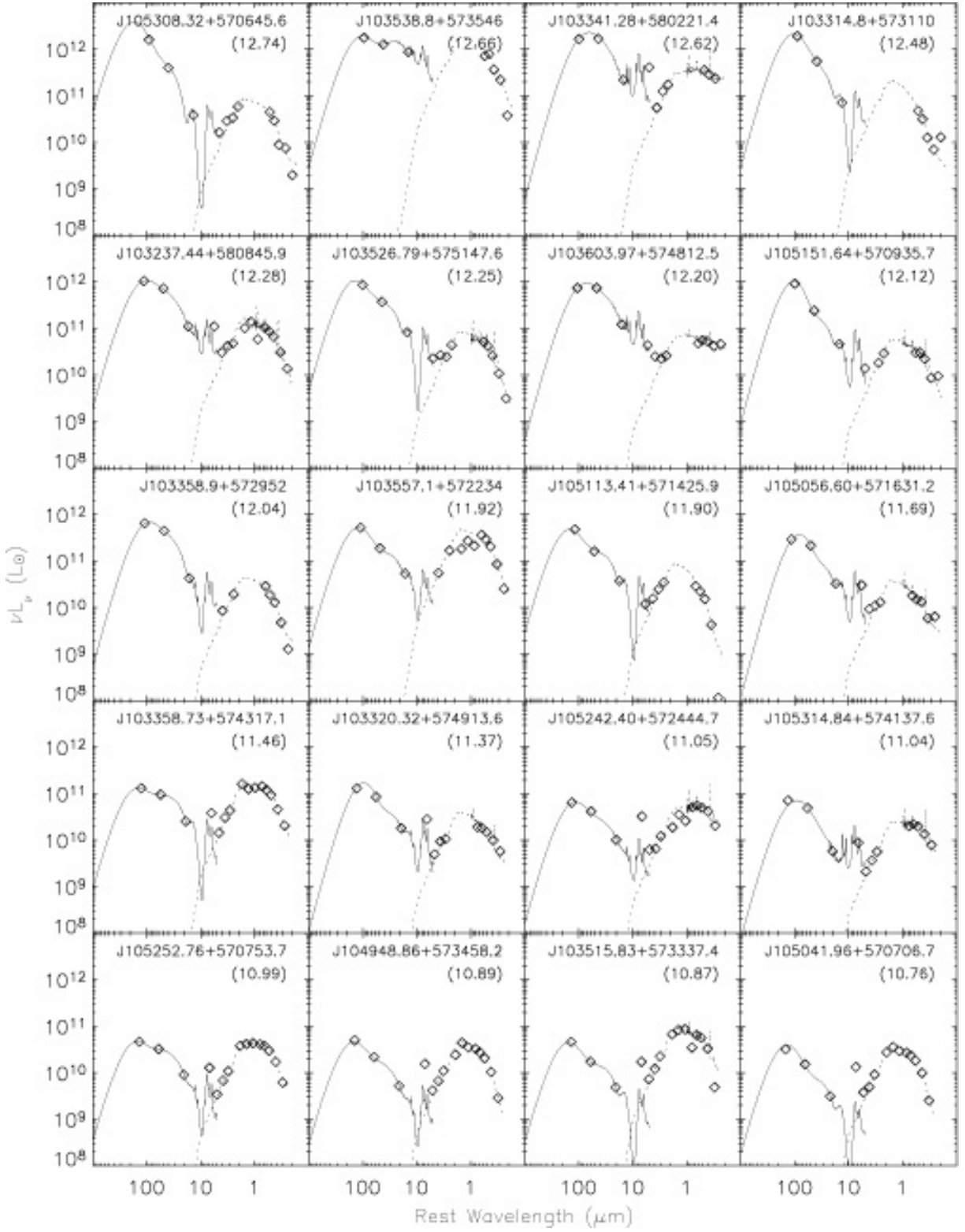


Fig. 6.— SEDs of SWIRE 160 μ m sources in νL_ν in units of solar luminosity versus rest wavelength (increasing to the left). The solid line represents a Siebenmorgen & Krugel (2007) model fit to the MIPS and 8 μ m data, shown as diamonds. The dotted line represents the stellar component of the luminosity and is fit to the shorter wavelength data (Ilbert et al. 2010). Sources are sorted by decreasing IR luminosity. We list the total-IR luminosity in each panel in units of $\log(L_{\text{IR}}/L_\odot)$ in parentheses below the source ID.

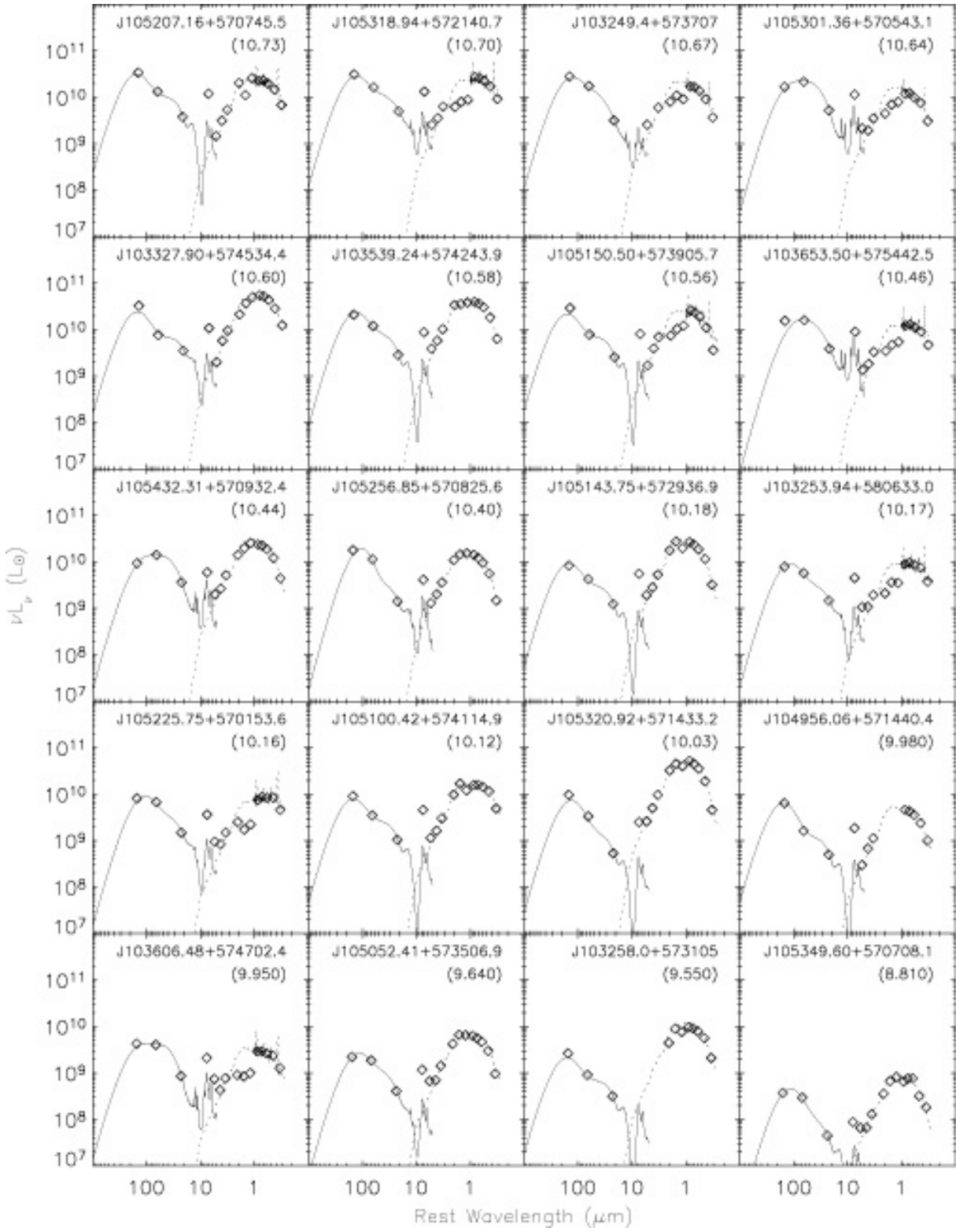


Figure 6 (Continued).

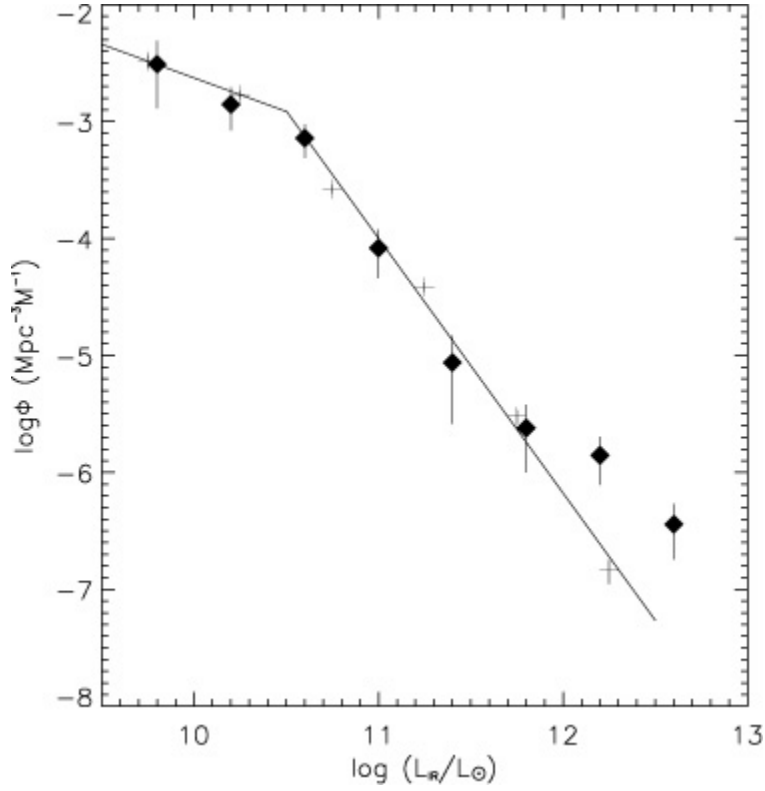


Fig. 7.— Infrared galactic LF from observations of the LH by SWIRE are shown as filled diamonds with 68% uncertainty bars. The RBGS data are shown as pluses fit by two power-laws (Sanders et al. 2003). At $\log(L_{\text{IR}}/L_{\odot}) = 9.5-10.5$ the RBGS is fit with $\Phi(L) \propto L^{-0.6 \pm 0.1}$, and at $\log(L_{\text{IR}}/L_{\odot}) = 10.5 - 12.5$ the power-law is: $\Phi(L) \propto L^{-2.2 \pm 0.1}$.

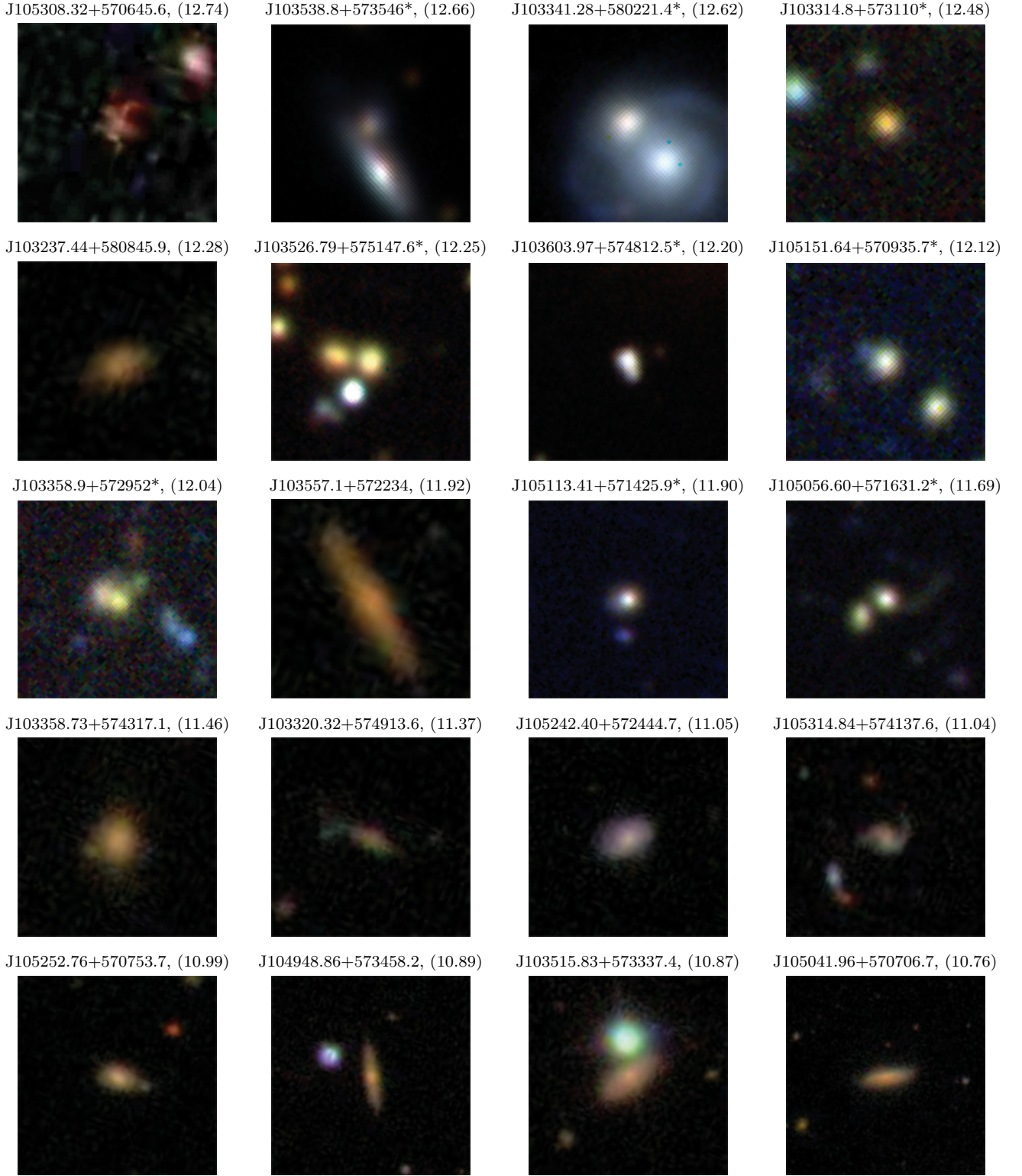


Fig. 8.— Stacked images of the LH sources sorted by luminosity. Most images are from SDSS finding charts, however for sources at $z > 0.3$ we show stacked KPNO $g'+r'+i'$ images when available, because these reveal more detail than SDSS (these images are marked with an asterisk). Images are oriented with North up and East to the left, with dimensions of $100 \text{ kpc} \times 100 \text{ kpc}$. We list the total-IR luminosity for each source in units of $\log(L_{\text{IR}}/L_{\odot})$ in parentheses following the source ID.

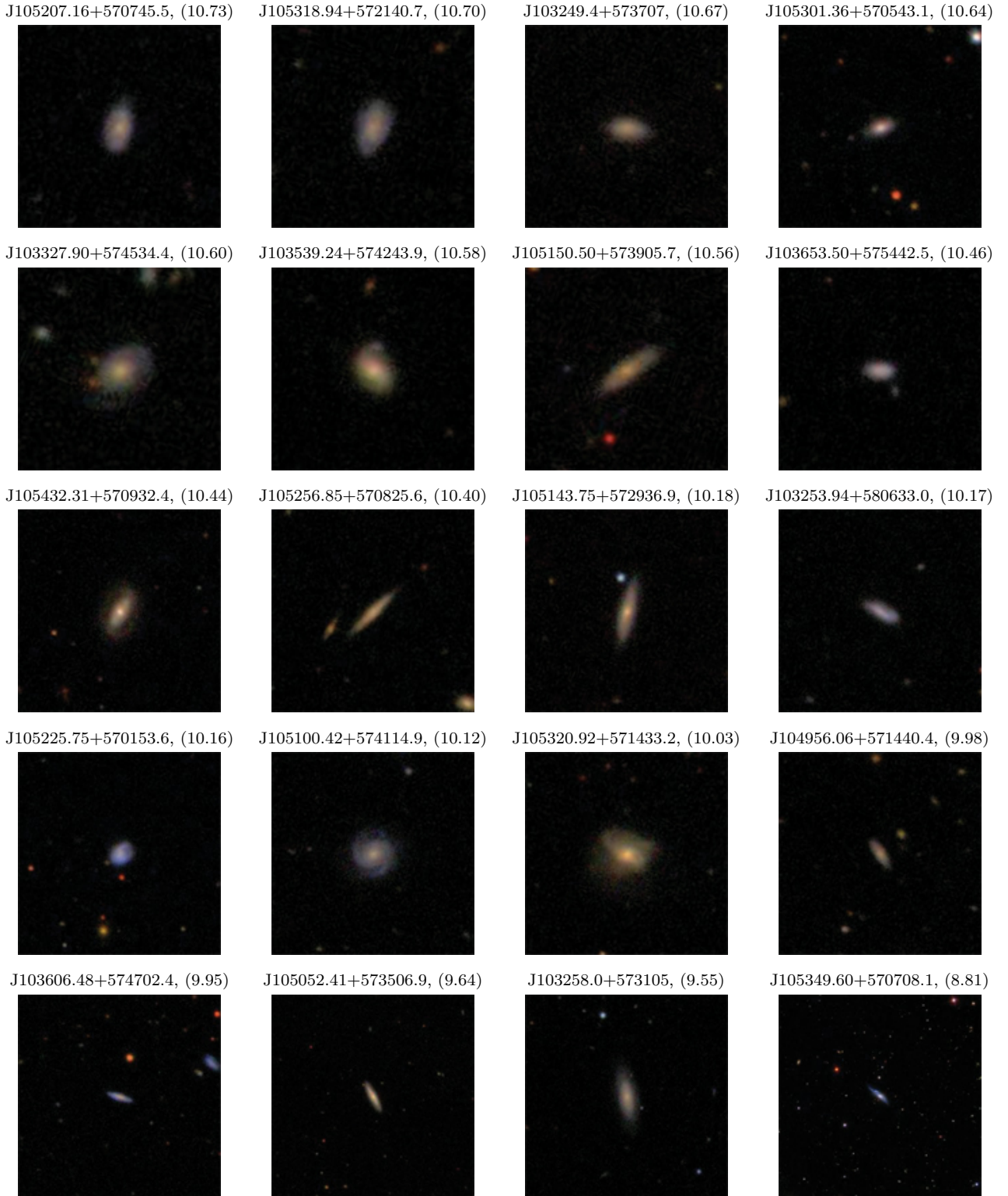


Figure 8 (Continued).

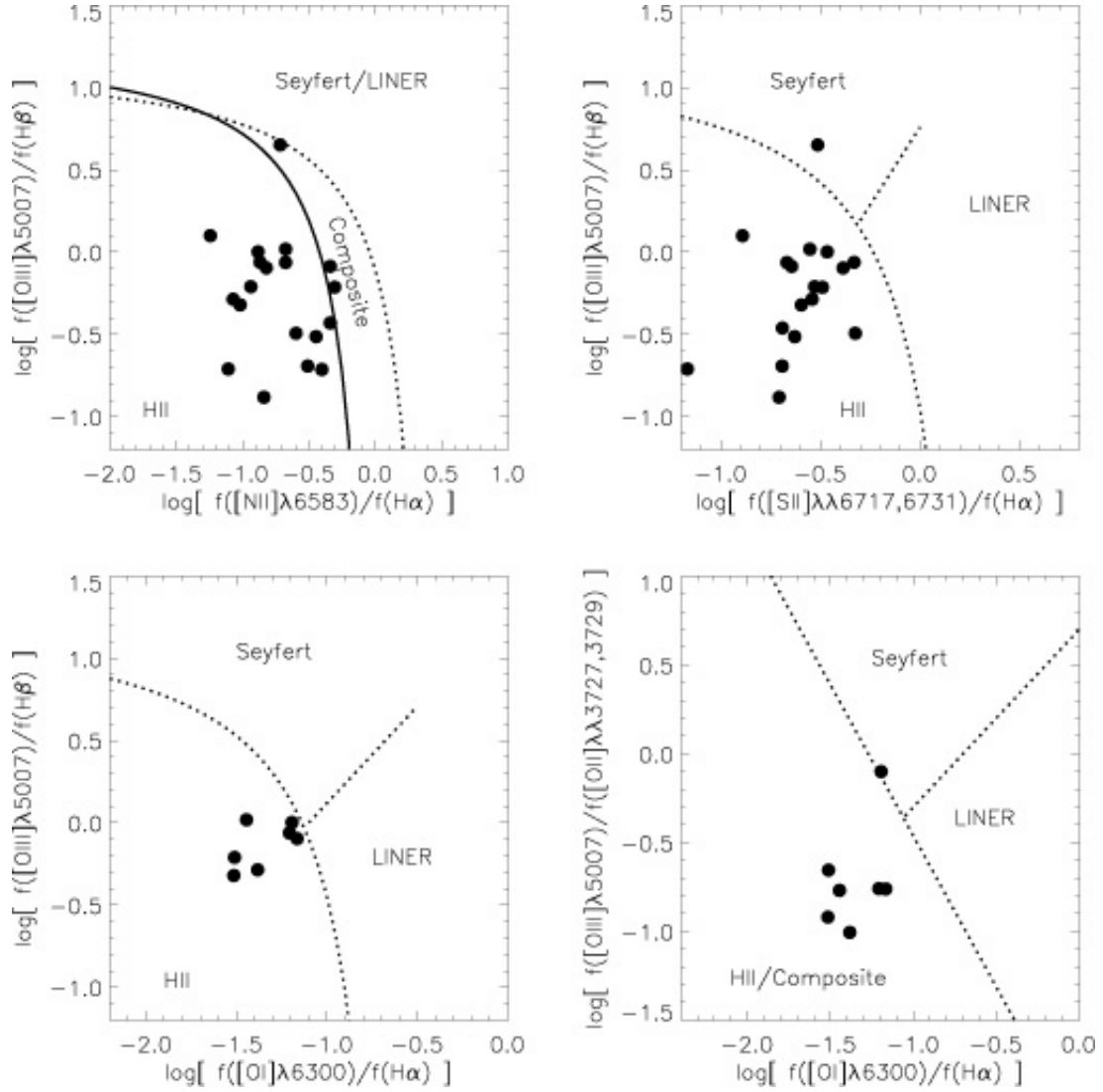


Fig. 9.— Optical spectral diagnostics, following the formalism of Kewley et al. (2006), for those sources with optical spectra and for which we were able to measure the relevant diagnostic lines. The dotted lines divide the diagrams into spectral classification types, and the solid line denotes the limit to pure star formation.

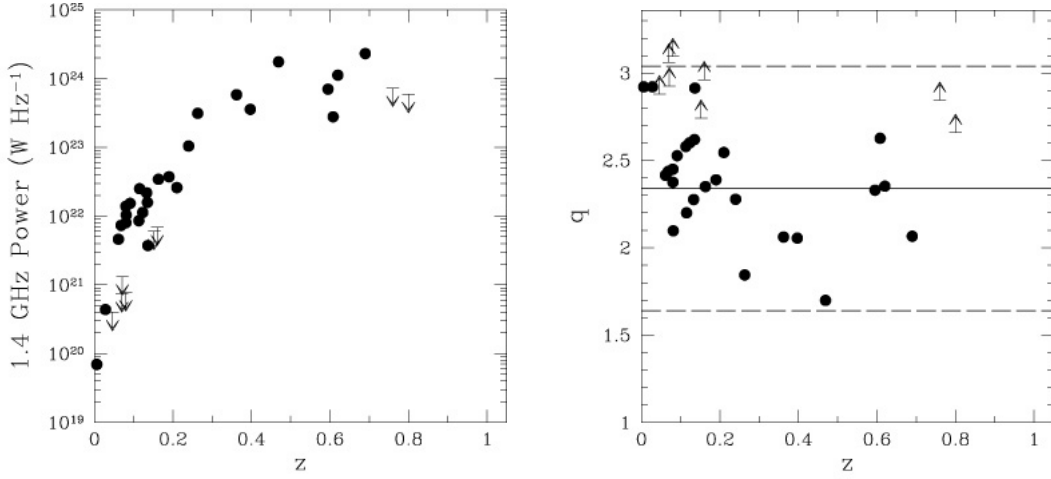


Fig. 10.— Left panel: 1.4 GHz radio power of the 34 sources with available radio data shown as a function of their redshifts. Right panel: The radio-FIR correlation q -value of the same 34 sources are shown. The solid horizontal line corresponds to $q = 2.34$, which is the mean of the local star forming galaxies, while the lower and upper dashed lines mark the radio-excess and IR-excess objects, respectively (see: Yun et al. 2001b).

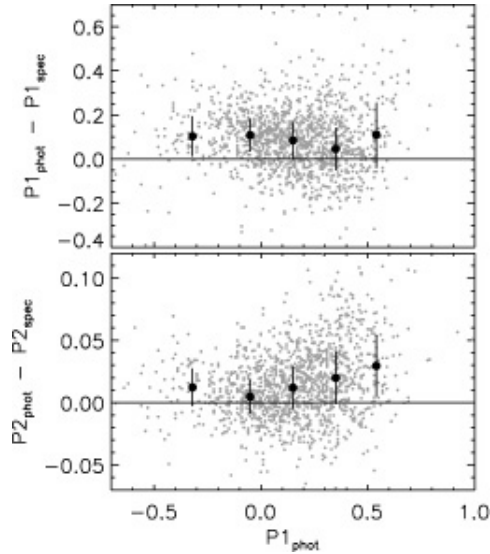


Fig. 11.— Offsets between the photometrically and spectroscopically derived P1 and P2 colors as a function of the former for a sample of ~ 1350 SDSS-IRAS galaxies (small gray dots). The former were obtained via SED fitting to the SDSS *ugriz* photometry using 100,000 model spectra from the Bruzual & Charlot (2003) library. The latter were derived from SDSS spectra as described in Smolčić et al. (2006). The large dots represent median offsets as a function of the photometrically derived P1 color. The error bars show the interquartile ranges.

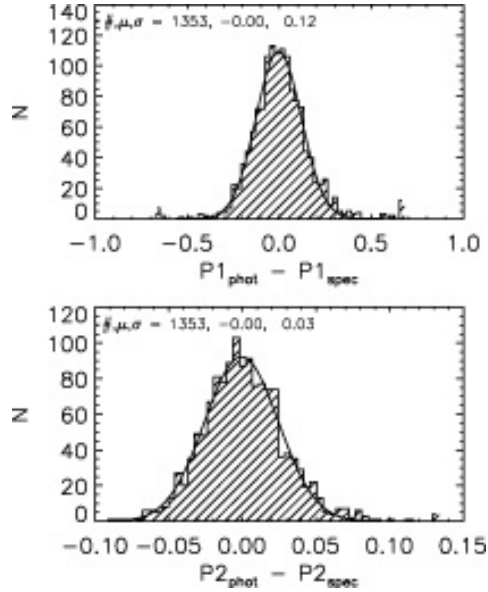


Fig. 12.— Distribution of the photometrically and spectroscopically derived P1 and P2 colors after the systematic offset correction (shown in Figure 11) was applied. The number of objects, mean, and standard deviation, as well as the best Gaussian fit are also shown in the panels.

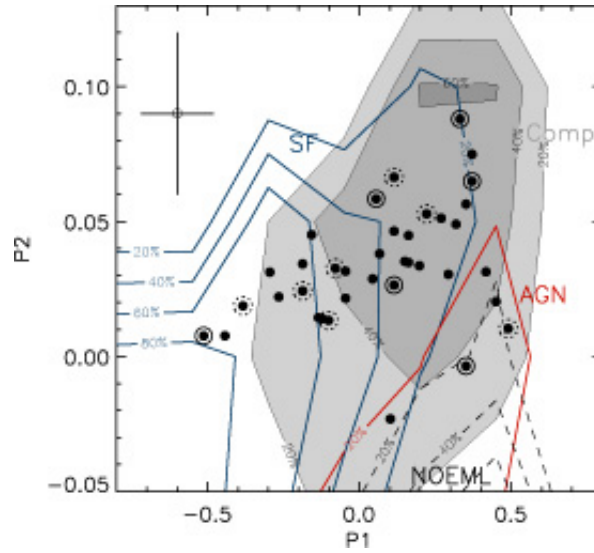


Fig. 13.— P1 vs. P2 color plane. The colors for the Lockman galaxies (after the corrections for systematics have been applied) are shown by large dots. Sources with $11 < \log L_{\text{IR}}/L_{\odot} < 12$ and $\log L_{\text{IR}}/L_{\odot} > 12$ are encircled with dashed and full lines, respectively. Contours represent the absorption (i.e. galaxies with no emission lines; NOEML), star forming, composite and AGN probability levels given a (P1,P2) combination (see text for details). The uncertainties in the P1 and P2 colors obtained via SED fitting are shown in the top left of the panel (see also Figure 12). Note, however, that the P2 error is likely lower than indicated in the panel (see text for details).

Table 1. Source List and Catalog Cross-Identification

#	Source		RA (J2000)	DEC (J2000)	160 μ m	70 μ m	IRAC+24 μ m		NIR (2MASS ID ²)	Optical (SDSS ID)	C_90	C_160
	(SWIRE ID ¹)	(J2000)					(SWIRE IDs)	(ISO ID)				
1	SWIRE3_J103237.44+580845.9	10 32 37.45	58 08 46.0	797	1989	...	620978	PSC:10323767+5808446	587729388220776605	
2	SWIRE2_24_J103249.4+573707	10 32 49.48	57 37 07.8	938	2338	3313	...	PSC:10324949+5737081	587729387683840107	INW192	2NW003	
3	SWIRE3_J103253.94+580633.0	10 32 53.95	58 06 33.1	804	2006	...	620883	PSC:10325395+5806333	587729388220776539	
4	SWIRE2_24_J103258.0+573105	10 32 58.02	57 31 05.3	974	...	2395	...	XSC:10325794+5731068	587732582590513271	
5	SWIRE2_24_J103314.8+573110	10 33 14.88	57 31 10.5	964	2385	2684	587732582590513949	
6	SWIRE3_J103320.32+574913.6	10 33 20.33	57 49 13.6	868	2177	...	463679	...	587732583127449867	INW021	2NW005	
7	SWIRE3_J103327.90+574534.4	10 33 27.91	57 45 34.5	887	462097	XSC:10332785+5745351	587729387683905620	
8	SWIRE3_J103341.28+580221.4	10 33 41.29	58 02 21.4	805	2013	...	472711	...	587732583127515249	...	2NW004	
9	SWIRE3_J103358.73+574317.1	10 33 58.73	57 43 17.2	891	2211	...	462979	XSC:10335869+5743169	587729387683905627	INW030	...	
10	SWIRE2_24_J103358.9+572952	10 33 58.92	57 29 52.3	945	2356	3540	587732582590578995	INW272	2NW009	
11	SWIRE3_J103515.83+573337.4	10 35 15.84	57 33 37.5	903	2253	...	462870	XSC:10351578+5733375	587732582590644271	
12	SWIRE3_J103526.79+575147.6	10 35 26.80	57 51 47.6	807	2034	...	473946	...	587729387683971243	
13	SWIRE2_24_J103538.8+573546	10 35 38.87	57 35 46.1	884	2209	7870	587732582590644410	
14	SWIRE3_J103539.24+574243.9	10 35 39.24	57 42 43.9	851	2117	...	469789	XSC:10353919+5742444	587732582590644435	
15	SWIRE2_24_J103557.1+572234	10 35 57.12	57 22 34.1	941	2340	5113	...	PSC:10355706+5722341	587729387147100345	
16	SWIRE3_J103603.97+574812.5	10 36 03.97	57 48 12.6	811	2038	...	474542	...	587729387684036627	INW092	...	
17	SWIRE3_J103606.48+574702.4	10 36 06.48	57 47 02.5	812	2052	...	474042	PSC:10360650+5747024	587729387684036713	INW023	...	
18	SWIRE3_J103653.50+575442.5	10 36 53.50	57 54 42.6	773	1935	...	481645	PSC:10365355+5754426	587729387684102266	
19	SWIRE3_J104948.86+573458.2	10 49 48.87	57 34 58.3	558	1482	...	228325	XSC:10494884+5734579	587729386611015724	
20	SWIRE3_J104956.06+571440.4	10 49 56.07	57 14 40.5	652	216021	...	587729386074079354	
21	SWIRE3_J105041.96+570706.7	10 50 41.96	57 07 06.8	673	1741	...	215353	XSC:10504192+5707064	587732580980818115	1EX048	2EX004	
22	SWIRE3_J105052.41+573506.9	10 50 52.41	57 35 07.0	534	1401	...	233199	XSC:10505236+5735064	587732581517754577	1EX041	2EX013	
23	SWIRE3_J105056.60+571631.2	10 50 56.60	57 16 31.2	625	1638	...	222478	...	587729386074145329	1EX085	2EX068	
24	SWIRE3_J105100.42+574114.9	10 51 00.43	57 41 15.0	512	1338	...	237144	XSC:10510035+5741153	587729386611081359	
25	SWIRE3_J105113.41+571425.9	10 51 13.41	57 14 26.0	617	1642	...	222633	...	587729386074145391	1EX081	2EX115	
26	SWIRE3_J105143.75+572936.9	10 51 43.75	57 29 36.9	544	1420	...	234071	XSC:10514374+5729367	587732581517754609	
27	SWIRE3_J105150.50+573905.7	10 51 50.51	57 39 05.7	499	239860	PSC:10515055+5739054	587729386611146842	
28	SWIRE3_J105151.64+570935.7	10 51 51.64	57 09 35.7	634	72224	...	587732580980883908	1EX047	2EX036	
29	SWIRE3_J105207.16+570745.5	10 52 07.16	57 07 45.6	635	1667	...	72439	XSC:10520715+5707445	587732580980883557	1EX034	2EX016	
30	SWIRE3_J105225.75+570153.6	10 52 25.76	57 01 53.7	653	1703	...	70615	PSC:10522572+5701537	587732580980883560	
31	SWIRE3_J105242.40+572444.7	10 52 42.40	57 24 44.8	542	1413	...	235900	PSC:10524240+5724447	587729386074276002	
32	SWIRE3_J105252.76+570753.7 ³	10 52 52.77	57 07 53.8	...	1607	...	76811	XSC:10525283+5707537	587732580980949106	1EX028	...	
33	SWIRE3_J105256.85+570825.6	10 52 56.85	57 08 25.7	603	1606	...	77421	XSC:10525689+5708257	587732580980949119	1EX269	2EX047	

Table 1—Continued

#	Source (SWIRE ID ¹)	RA (J2000)	DEC (J2000)	160 μ m	70 μ m	24 μ m	IRAC+24 μ m	NIR (2MASS ID ²)	Optical (SDSS ID)	C_90	C_160
34	SWIRE3_J105301.36+570543.1	10 53 01.36	57 05 43.2	611	1629	...	76215	PSC:10530133+5705433	587732580980949116	1EX062	...
35	SWIRE3_J105308.32+570645.6	10 53 08.32	57 06 45.6	610	77408	...	587732580980949913
36	SWIRE3_J105314.84+574137.6	10 53 14.85	57 41 37.7	447	1202	...	247971	...	587732581517885646
37	SWIRE3_J105318.94+572140.7	10 53 18.94	57 21 40.7	538	1407	...	86339	PSC:10531899+5721394	587729386074276027	1EX179	...
38	SWIRE3_J105320.92+571433.2	10 53 20.92	57 14 33.3	568	1498	...	82519	XSC:10532085+5714338	587732580980949157	1EX126	...
39	SWIRE3_J105349.60+570708.1	10 53 49.60	57 07 08.1	582	1562	...	80766	XSC:10534950+5707075	587732580980949076
40	SWIRE3_J105432.31+570932.4	10 54 32.31	57 09 32.5	559	1478	...	85419	XSC:10543226+5709324	587732580981014580

Note. — Sources in the LHNW and LHEX fields. The columns list a counter number, SWIRE Source ID, right ascension and declination (HH MM SS.SS and DD MM SS.S) taken from the SWIRE IRAC+24 μ m when available, ID counter numbers from the SWIRE 160 μ m, 70 μ m, 24 μ m, and IRAC+24 μ m catalogs, 2MASS source designation and catalog, object ID from SDSS, and the ISO-LH 90 μ m and 160 μ m source ID from Oyabu et al. (2005).

¹SWIRE2_24-J103249.4+573707, J103258.0+573105, J103314.8+573110, J103358.9+572952, J103538.8+573546, and J103557.1+572234 lack entries in the SWIRE IRAC+24 μ m catalog so their RA, DEC and 24 μ m flux are taken from the independent SWIRE 24 μ m catalog

²Preceding the 2MASS source designation are the reference catalog abbreviations, PSC for the 2MASS Point Source Catalog, and XSC for the Extended Source Catalog. Values from the XSC are preferred when available.

³SWIRE3_J105252.76+570753.7 was not included in the SWIRE 160 μ m catalog, but was visible in the image, and detected by ISO so we independently measure its flux by hand.

Table 2. Source Photometry

#	Source	(mJy)										(mag)								
		20cm	160 μ m	70 μ m	24 μ m	8 μ m	5.8 μ m	4.5 μ m	3.6 μ m	Ks	H	J	i'	r'	g'	z	i	r	g	u
1	SWIRE3_J103237.44+580845.9	...	390	117	6.17	2.051	0.409	0.437	0.401	17.13	17.09	18.32	18.02	18.43	18.95	20.07	21.33
2	SWIRE2_24_J103249.4+573707	0.638	193	52.7	3.26	...	0.641	...	0.931	16.72	16.67	17.17	16.79	17.05	17.47	18.22	19.57
3	SWIRE3_J103253.94+580633.0	...	142	45.1	3.96	4.067	0.697	0.550	0.785	17.12	16.82	17.15	16.44	16.61	16.93	17.39	18.50
4	SWIRE2_24_J103258.0+573105	< 0.078	124	18.6	2.23	15.27	14.80	15.27	15.32	15.61	15.99	16.65	18.10
5	SWIRE2_24_J103314.8+573110	< 0.074	150	18.9	0.84	20.55	21.22	22.44	23.37	23.07
6	SWIRE3_J103320.32+574913.6	0.437	176	50.3	3.65	1.899	0.243	0.357	0.324	18.53	18.97	19.83	18.45	18.71	19.16	19.90	20.85
7	SWIRE3_J103327.90+574534.4	< 0.079	122	12.5	1.97	2.014	0.272	0.610	0.800	16.31	16.01	15.98	16.88	17.12	17.90	16.20	16.48	16.88	17.65	18.91
8	SWIRE3_J103341.28+580221.4	0.315	242	108	4.79	2.976	0.292	0.515	0.567	17.90	18.35	18.88	20.99	21.66	21.16	22.70	22.38
9	SWIRE3_J103358.73+574317.1	1.027	144	45.9	4.18	2.093	0.572	0.942	1.088	15.44	16.01	16.24	17.03	17.48	18.61	16.48	16.89	17.38	18.46	19.70
10	SWIRE2_24_J103358.9+572952	1.146	185	55.7	1.83	...	0.088	...	0.124	19.69	20.36	21.00	22.38	24.18
11	SWIRE3_J103515.83+573337.4	< 0.080	153	25.3	2.42	2.875	0.879	1.144	1.714	15.20	15.25	15.52	16.88	17.15	17.95	16.81	16.36	16.71	17.61	20.05
12	SWIRE3_J103526.79+575147.6	0.224	139	26.3	2.01	0.183	0.155	0.111	0.159	19.85	20.38	21.57	19.67	20.13	20.86	22.12	23.82
13	SWIRE2_24_J103538.8+573546	0.465	199	62.9	14.8	17.20	17.32	18.38	19.23	21.51
14	SWIRE3_J103539.24+574243.9	0.227	150	37.4	3.04	3.130	1.001	1.171	1.645	15.12	15.36	15.57	16.05	16.46	17.30	15.85	16.16	16.59	17.43	18.94
15	SWIRE2_24_J103557.1+572234	...	156	24.4	2.41	...	0.600	...	1.129	16.73	16.59	17.16	16.88	17.34	17.95	19.19	20.88
16	SWIRE3_J103603.97+574812.5	...	172	75.5	4.26	0.507	0.210	0.147	0.136	19.42	19.74	20.30	19.36	19.42	19.68	20.24	20.51
17	SWIRE3_J103606.48+574702.4	...	220	91.3	6.65	5.419	1.384	0.619	0.898	16.90	17.27	17.39	16.79	17.03	17.44	16.53	16.76	17.08	17.51	18.53
18	SWIRE3_J103653.50+575442.5	...	137	62.3	5.17	3.985	0.434	0.455	0.664	17.35	17.30	17.46	17.12	17.41	17.98	16.88	17.06	17.42	17.96	19.03
19	SWIRE3_J104948.86+573458.2	0.276	242	45.9	3.77	3.756	0.730	0.915	1.200	15.89	15.53	16.09	17.15	17.63	18.52	16.48	16.88	17.42	18.46	20.21
20	SWIRE3_J104956.06+571440.4	< 0.058	126	14.0	1.48	1.830	0.213	0.374	0.501	17.43	17.78	18.49	17.08	17.38	17.79	18.54	19.84
21	SWIRE3_J105041.96+570706.7	0.669	362	75.2	5.30	7.510	1.552	1.587	2.330	14.84	14.84	15.36	16.10	16.46	17.37	15.77	16.15	16.64	17.59	19.44
22	SWIRE3_J105052.41+573506.9	0.245	288	106	7.97	7.632	3.171	2.581	4.199	14.22	14.02	14.35	14.99	15.32	16.11	14.69	15.03	15.45	16.24	17.83
23	SWIRE3_J105056.60+571631.2	0.379	124	39.8	2.10	0.639	0.142	0.131	0.124	20.15	20.37	21.71	19.77	20.20	20.53	21.73	22.00
24	SWIRE3_J105100.42+574114.9	< 0.100	174	29.1	3.00	4.375	0.795	0.879	1.298	15.40	15.09	15.75	15.88	16.11	16.66	15.78	15.99	16.31	16.87	18.14
25	SWIRE3_J105113.41+571425.9	0.802	250	37.4	2.95	0.313	0.295	0.370	0.414	19.48	20.09	21.71	19.03	19.51	20.15	21.84	26.13
26	SWIRE3_J105143.75+572936.9	0.588	121	26.9	2.68	4.030	1.009	1.146	1.725	15.05	14.86	15.53	16.03	16.47	17.15	15.52	15.86	16.34	17.16	18.89
27	SWIRE3_J105150.50+573905.7	0.064	139	16.4	1.82	1.918	0.296	0.531	0.747	17.19	17.13	17.25	16.94	17.34	18.22	16.73	17.07	17.53	18.41	19.99
28	SWIRE3_J105151.64+570935.7	0.083	140	16.1	1.06	0.106	...	0.078	0.100	20.40	20.90	22.15	20.32	20.53	21.10	22.42	22.68
29	SWIRE3_J105207.16+570745.5	0.246	202	34.6	3.37	3.563	0.314	0.524	0.715	15.87	16.81	16.20	16.66	16.86	17.24	17.86	19.06
30	SWIRE3_J105225.75+570153.6	0.490	213	77.3	5.85	4.769	0.901	0.615	0.885	16.52	17.22	17.24	16.24	16.30	16.55	16.86	17.87
31	SWIRE3_J105242.40+572444.7	0.283	147	41.3	3.47	3.711	0.517	0.420	0.625	16.98	16.59	17.23	16.79	16.94	17.26	17.78	18.90
32	SWIRE3_J105252.76+570753.7	0.381	149	45.4	4.34	2.048	0.399	0.611	0.781	15.86	16.05	16.31	16.69	16.99	17.47	18.36	19.84
33	SWIRE3_J105256.85+570825.6	0.467	266	74.1	3.15	3.070	0.702	0.847	1.212	15.54	15.51	15.77	16.17	16.55	17.03	17.92	19.73

Table 2—Continued

#	Source	20cm	160 μ m	70 μ m	24 μ m	8 μ m	5.8 μ m	4.5 μ m	3.6 μ m	<i>Ks</i>	<i>H</i>	<i>J</i>	<i>i'</i>	<i>r'</i>	<i>g'</i>	<i>z</i>	<i>i</i>	<i>r</i>	<i>g</i>	<i>u</i>	
	(SWIRE ID)				(mJy)								(mag)								
34	SWIRE3_J105301.36+570543.1	0.809	249	142	11.7	8.517	1.159	0.817	1.176	16.51	16.32	16.48	16.35	16.54	17.00	17.59	18.93	
35	SWIRE3_J105308.32+570645.6	< 0.107	142	15.5	0.51	0.072	0.092	0.084	0.118	—	—	—	20.48	21.16	22.68	23.15	24.97	
36	SWIRE3_J105314.84+574137.6	0.153	131	39.1	1.58	0.810	0.140	0.189	0.232	—	—	—	18.11	18.34	19.07	18.05	18.18	18.52	19.24	20.19	
37	SWIRE3_J105318.94+572140.7	0.394	156	36.1	3.75	3.338	0.464	0.505	0.713	17.33	17.35	17.55	16.64	16.91	17.27	17.88	18.91	
38	SWIRE3_J105320.92+571433.2	< 0.045	144	21.6	1.19	1.863	1.392	2.110	3.230	14.37	14.30	14.72	14.75	15.13	15.61	16.59	18.50	
39	SWIRE3_J105349.60+570708.1	0.911	1087	379	19.8	12.89	6.983	5.458	8.529	13.52	13.13	13.21	13.76	13.83	14.03	15.28	16.25	
40	SWIRE3_J105432.31+570932.4	0.614	195	129	11.4	6.200	1.518	1.569	2.426	14.90	14.82	14.84	15.23	15.52	15.93	16.69	18.15	

Note. — Source photometry in the LHNW and LHEX fields listed in order of right ascension. The columns list a counter number, the source ID, the 20 cm VLA flux, the flux in the Spitzer wavelengths in mJy, and 2MASS *JHK_s*-bands, SWIRE *i'r'g'*-bands and SDSS *z'rg'u*-bands in AB magnitudes. Sources without listed values (...) in Spitzer-IRAC and/or the SWIRE/NOAO *i'r'g'*-bands were typically located on the edge of the LHNW field not covered by SWIRE (see Figure 1). Sources without 2MASS photometry (—) were not found in the 2MASS photometry catalog.

Table 3. Redshift and Infrared Luminosity

#	Source	z	z -Ref.	$\log(L_{\text{IR}})$ (L_{\odot})	$\log(L_{1.4\text{GHz}})$ (W Hz $^{-1}$)
1	SWIRE3_J103237.44+580845.9*	0.42 ± 0.02	Phot-z	12.28 ± 0.05	...
2	SWIRE2_24_J103249.4+573707	0.115	ESI/ech	10.67	22.40
3	SWIRE3_J103253.94+580633.0	0.073	SDSS	10.17	...
4	SWIRE2_24_J103258.0+573105	0.046	SDSS	9.55	< 20.60
5	SWIRE2_24_J103314.8+573110*	$0.80^{+0.22}_{-0.18}$	Phot-z	$12.48^{+0.26}_{-0.27}$	< 23.77
6	SWIRE3_J103320.32+574913.6	0.240	ESI/ech	11.37	23.02
7	SWIRE3_J103327.90+574534.4	0.152	SDSS	10.60	< 21.78
8	SWIRE3_J103341.28+580221.4*	$0.62^{+0.06}_{-0.08}$	Phot-z ²	$12.62^{+0.10}_{-0.15}$	24.05
9	SWIRE3_J103358.73+574317.1	0.263	ESI/ech	11.46	23.49
10	SWIRE2_24_J103358.9+572952	0.469	ESI/ech	12.04	24.24
11	SWIRE3_J103515.83+573337.4*	0.16 ± 0.02	Phot-z	10.87 ± 0.12	< 21.84
12	SWIRE3_J103526.79+575147.6	0.595	ESI/low-d	12.25	23.85
13	SWIRE2_24_J103538.8+573546*	0.69 ± 0.03	Phot-z	$12.66^{+0.05}_{-0.04}$	24.36
14	SWIRE3_J103539.24+574243.9	0.113	ESI/ech	10.58	21.93
15	SWIRE2_24_J103557.1+572234*	$0.46^{+0.02}_{-0.26}$	Phot-z	$11.92^{+0.04}_{-0.84}$...
16	SWIRE3_J103603.97+574812.5 ¹	0.511	B ¹	12.20	...
17	SWIRE3_J103606.48+574702.4	0.044	SDSS	9.95	...
18	SWIRE3_J103653.50+575442.5	0.102	SDSS	10.46	...
19	SWIRE3_J104948.86+573458.2	0.135	SDSS+ESI/low-d	10.89	22.20
20	SWIRE3_J104956.06+571440.4*	0.07 ± 0.03	Phot-z	$9.98^{+0.37}_{-0.46}$	< 20.87
21	SWIRE3_J105041.96+570706.7	0.091	ESI/ech	10.76	22.18
22	SWIRE3_J105052.41+573506.9	0.028	SDSS+ESI/ech	9.64	20.64
23	SWIRE3_J105056.60+571631.2	0.397	ESI/low-d	11.69	23.55
24	SWIRE3_J105100.42+574114.9	0.071	ESI/ech	10.12	< 21.12
25	SWIRE3_J105113.41+571425.9	0.362	ESI/ech	11.90	23.76
26	SWIRE3_J105143.75+572936.9	0.081	ESI/ech	10.18	22.01
27	SWIRE3_J105150.50+573905.7	0.136	SDSS	10.56	21.57
28	SWIRE3_J105151.64+570935.7	0.608	ESI/low-d	12.12	23.44
29	SWIRE3_J105207.16+570745.5	0.123	ESI/ech	10.73	22.05
30	SWIRE3_J105225.75+570153.6	0.061	ESI/ech	10.16	21.66
31	SWIRE3_J105242.40+572444.7*	$0.19^{+0.01}_{-0.03}$	Phot-z	$11.05^{+0.07}_{-0.15}$	22.57
32	SWIRE3_J105252.76+570753.7	0.163	SDSS+ESI/low-d	10.99	22.53
33	SWIRE3_J105256.85+570825.6	0.080	ESI/low-d	10.40	21.90
34	SWIRE3_J105301.36+570543.1	0.080	ESI/ech	10.64	22.14
35	SWIRE3_J105308.32+570645.6*	$0.76^{+0.14}_{-0.26}$	Phot-z	$12.74^{+0.19}_{-0.44}$	< 23.86
36	SWIRE3_J105314.84+574137.6*	$0.21^{+0.05}_{-0.03}$	Phot-z	$11.04^{+0.21}_{-0.15}$	22.41
37	SWIRE3_J105318.94+572140.7	0.133	SDSS	10.70	22.34
38	SWIRE3_J105320.92+571433.2	0.080	SDSS	10.03	< 20.89
39	SWIRE3_J105349.60+570708.1 ¹	0.006	NED ¹	8.81	19.84
40	SWIRE3_J105432.31+570932.4	0.068	SDSS	10.44	21.86

Note. — Sources in the LHNW and LHEX fields listed in order of increasing right ascension, with columns giving a counter number, source ID, redshift, infrared luminosity (8-1000 μ m) in units of L_{\odot} , and radio power $L_{1.4\text{GHz}}$ in units: $\log(\text{W Hz}^{-1})$. The sources of the spectra listed in the z -Ref. column are: from ESI on Keck II in low-dispersion (low-d) and echellette (ech) mode, from Amy Barger’s private communication (2003) (B), from SDSS, and from NED.

*Sources without existing optical spectra, for which we have determined photometric redshifts (see text and Figure 6). The computed phot-z value, and 68% uncertainty is listed. This uncertainty was propagated when computing the listed infrared luminosity.

¹Thirty of the forty sources in our sample have spectroscopic redshifts, and 28 of these have spectra, which are displayed in Figures 5.1 – 5.28. The spectra for sources J103603.97+574812.5, and J105349.60+570708.1 are not available.

²For the case of J103341.28+580221.4, we prefer the SWIRE optical data due to confusion with a foreground spiral and use these rather than the SDSS data to calculate its photometric redshift.

Table 4. Luminosity Function

$\log(L_{\text{IR}})$ (L_{\odot})	Φ ($\text{Mpc}^{-3} \text{ mag}^{-1}$)	σ_{Φ}	V/V_{max}	$\sigma_{V/V_{\text{max}}}$	Number	Median z
9.8	3.1×10^{-3}	1.8×10^{-3}	0.53	0.11	3	0.044
10.2	1.4×10^{-3}	5.6×10^{-4}	0.64	0.09	6	0.077
10.6	7.2×10^{-4}	2.3×10^{-4}	0.59	0.07	10	0.114
11.0	8.3×10^{-5}	3.7×10^{-5}	0.68	0.11	5	0.163
11.4	8.7×10^{-6}	6.1×10^{-6}	0.66	0.17	2	0.251
11.8	2.4×10^{-6}	1.4×10^{-6}	0.65	0.13	3	0.397
12.2	1.4×10^{-6}	6.2×10^{-7}	0.57	0.09	5	0.511
12.6	3.6×10^{-7}	1.8×10^{-7}	0.58	0.10	4	0.725

Note. — The galaxy sample is placed into luminosity bins of 0.4 in the range $\log(L_{\text{IR}}/L_{\odot})$. We list the space density Φ , the uncertainty in this value, volume sampling parameter V/V_{max} , uncertainty in V/V_{max} , the number of galaxies in each bin, and the median redshift.

Table 5. Spectral Properties, Masses and Morphologies

#	Source	$\log(L_{\text{IR}})$ (L_{\odot})	$E(B-V)$	$12+\log[O/H]$	S-Type	q -value	$\log(M_*)$ (M_{\odot})	Morphology	Notes
35	SWIRE3_J105308.32+570645.6	$12.74^{+0.19}_{-0.44}$	> 2.84	10.90	Highly Disturbed	tidal features
13	SWIRE2_24_J103538.8+573546	$12.66^{+0.05}_{-0.04}$	2.07	*	Spheroid	S overlapping foreground galaxy with $z = 0.103$.
8	SWIRE3_J103341.28+580221.4	$12.62^{+0.15}_{-0.15}$	2.35	*	Spheroid	SW foreground spiral with $z = 0.075$.
5	SWIRE2_24_J103314.8+573110	$12.48^{+0.26}_{-0.27}$	> 2.66	11.25	Spheroid	
1	SWIRE3_J103237.44+580845.9	12.28 ± 0.05	11.18	Disk	disturbed, tidal features
12	SWIRE3_J103526.79+575147.6	12.25	...	H/C/L:	...	2.33	10.82	Spheroid	pair ($d = 20$ kpc, $\Delta z = 0.001$); star to S.
16	SWIRE3_J103603.97+574812.5	12.20	10.88	Merger	overlapping pair
28	SWIRE3_J105151.64+570935.7	12.12	...	S:	...	2.63	*	Spheroid	pair ? ($d = 30$ kpc)
10	SWIRE2_24_J103358.9+572952	12.04	1.70	10.75	Spheroid	tidal debris. (NE object is bkg source with $z = 0.837$.)
15	SWIRE2_24_J103557.1+572234	$11.92^{+0.04}_{-0.84}$	11.77	Disk	large (100 kpc) edge-on disk
25	SWIRE3_J105113.41+571425.9	11.90	...	S/L:	...	2.06	11.49	Spheroid	compact
23	SWIRE3_J105056.60+571631.2	11.69	1.00	H:	...	2.06	10.63	Spheroid	tidal debris + pair ($d = 40$ kpc, $\Delta z = 0.001$)
9	SWIRE3_J103358.73+574317.1	11.46	0.88	H	...	1.84	11.70	Spheroid	faint SE companion ($d = 7$ kpc)
6	SWIRE3_J103320.32+574913.6	11.37	0.66	H	...	2.28	10.77	Disk	tidal arm(s).
31	SWIRE3_J105242.40+572444.7	$11.05^{+0.07}_{-0.15}$	2.39	10.86	Disk	
36	SWIRE3_J105314.84+574137.6	$11.04^{+0.21}_{-0.15}$	2.55	10.46	Disk	interacting system with SE companion ($d = 30$ kpc)
32	SWIRE3_J105252.76+570753.7	10.99	0.86	H	...	2.35	11.11	Disk	tidal feature - possible SW companion
19	SWIRE3_J104948.86+573458.2	10.89	...	C/S/L:	...	2.62	11.24	Disk	edge-on with bright nucleus
11	SWIRE3_J103515.83+573337.4	10.87 ± 0.12	> 2.96	11.04	Disk	bright star to N
21	SWIRE3_J105041.96+570706.7	10.76	2.08	H	...	2.53	11.19	Disk	edge-on
29	SWIRE3_J105207.16+570745.5	10.73	0.11	H	...	2.60	10.72	Disk	
37	SWIRE3_J105318.94+572140.7	10.70	0.53	H	...	2.28	10.88	Disk	
2	SWIRE2_24_J103249.4+573707	10.67	0.58	H	...	2.20	10.74	Disk	
34	SWIRE3_J105301.36+570543.1	10.64	0.47	H	...	2.38	10.49	Disk	compact with bright nucleus
7	SWIRE3_J103327.90+574534.4	10.60	0.71	H	> 2.74	> 2.74	11.25	Disk	possible tidal arm
14	SWIRE3_J103539.24+574243.9	10.58	0.71	H	...	2.58	11.03	Disk	small companion to N
27	SWIRE3_J105150.50+573905.7	10.56	2.91	10.95	Disk	edge-on
18	SWIRE3_J103653.50+575442.5	10.46	0.52	H	10.58	Disk	compact with possible companion to SW
40	SWIRE3_J105432.31+570932.4	10.44	0.74	H	...	2.44	10.88	Disk	bright nucleus
33	SWIRE3_J105256.85+570825.6	10.40	...	L:	...	2.45	10.80	Disk	edge-on with companion to SE
26	SWIRE3_J105143.75+572936.9	10.18	1.87	S	...	2.10	11.09	Disk	edge-on with bright nucleus
3	SWIRE3_J103253.94+580633.0	10.17	0.55	H	10.26	Disk	disturbed
30	SWIRE3_J105225.75+570153.6	10.16	0.14	H	...	2.42	10.04	Disk	blue compact

Table 5—Continued

#	Source	$\log(L_{\text{IR}})$ (L_{\odot})	$E(B - V)$	$12 + \log(O/H)$	S-Type	q -value	$\log(M_*)$ (M_{\odot})	Morphology	Notes
24	SWIRE3-J105100.42+574114.9	10.12	1.41	...	H	> 2.93	10.56	Disk	face-on
38	SWIRE3-J105320.92+571433.2	10.03	> 3.09	11.47	Disk	face-on, disturbed with bright nucleus
20	SWIRE3-J104956.06+571440.4	$9.98^{+0.37}_{-0.46}$	> 3.06	10.23	Disk	small, edge-on
17	SWIRE3-J103606.48+574702.4	9.95	0.55	8.58	H	...	9.70	Disk	small, edge-on
22	SWIRE3-J105052.41+573506.9	9.64	0.52	8.43	H	2.92	10.40	Disk	small, edge-on
4	SWIRE2.24-J103258.0+573105	9.55	0.49	9.00	H/C:	> 2.88	10.47	Disk	edge-on
39	SWIRE3-J105349.60+570708.1	8.81	2.92	9.45	Disk	blue compact

Note. — Sources in the LHNW and LHEX fields listed in order of decreasing L_{IR} . Columns give RA ordered counter number, source ID, infrared luminosity (8-1000 μm) in units of L_{\odot} , extinction, metallicity, spectral type (H = star-forming, C = star-forming + AGN, S = Seyfert, L = LINER), stellar mass estimates in $\log(M_{\odot})$ using the methods described in Ilbert et al. (2010), ‘ q -value’ of FIR-radio correlation, morphology, and Notes (tidal debris and/or companions). The spectral types are determined by use of the methods of Kewley et al. (2006), while the extinction is calculated using the Balmer decrement, and metallicities using the $[\text{NII}]/[\text{OII}]$ diagnostic of Kewley et al. (2002).

* Sources J103538.8+573546 and J103341.28+580221.4 suffer from contamination due to partially overlapping foreground galaxies, which prohibits determining accurate masses. Source J105151.64+570935.7 is spectroscopically classified as a Seyfert and is suspected to harbor a QSO, thus the use of *Le Phare* to determine a mass from the UV-NIR photometry is inappropriate.

Table 6. Spectral Type Probabilities from P1P2 Analysis

#	Source	$\log(L_{\text{IR}})$	P1 Color	P2 Color	SF	Comp.	AGN	No EML
		(L_{\odot})						
35	SWIRE3_J105308.32+570645.6	$12.74^{+0.19}_{-0.44}$	0.37	0.06	0.37	0.51	0.06	0.06
13	SWIRE2_24_J103538.8+573546*	$12.66^{+0.05}_{-0.04}$	*	*	*	*	*	*
8	SWIRE3_J103341.28+580221.4*	$12.62^{+0.10}_{-0.15}$	*	*	*	*	*	*
5	SWIRE2_24_J103314.8+573110	$12.48^{+0.26}_{-0.27}$	0.35	0.00	0.08	0.19	0.29	0.44
1	SWIRE3_J103237.44+580845.9	12.28 ± 0.05	0.11	0.03	0.54	0.31	0.10	0.04
12	SWIRE3_J103526.79+575147.6	12.25	0.05	0.06	0.43	0.53	0.04	0.00
16	SWIRE3_J103603.97+574812.5	12.20	-0.51	0.01	0.90	0.03	0.02	0.05
28	SWIRE3_J105151.64+570935.7*	12.12	*	*	*	*	*	*
10	SWIRE2_24_J103358.9+572952	12.04	0.33	0.09	0.37	0.51	0.06	0.06
15	SWIRE2_24_J103557.1+572234	$11.92^{+0.04}_{-0.84}$	0.22	0.05	0.37	0.51	0.06	0.06
25	SWIRE3_J105113.41+571425.9	11.90	0.49	0.01	0.06	0.33	0.36	0.24
23	SWIRE3_J105056.60+571631.2	11.69	-0.10	0.01	0.72	0.25	0.02	0.00
9	SWIRE3_J103358.73+574317.1	11.46	0.11	0.07	0.43	0.53	0.04	0.00
6	SWIRE3_J103320.32+574913.6	11.37	-0.08	0.03	0.72	0.25	0.02	0.00
31	SWIRE3_J105242.40+572444.7	$11.05^{+0.07}_{-0.15}$	-0.38	0.02	0.90	0.03	0.02	0.05
36	SWIRE3_J105314.84+574137.6	$11.04^{+0.21}_{-0.15}$	-0.19	0.02	0.72	0.25	0.02	0.00
32	SWIRE3_J105252.76+570753.7	10.99	0.11	0.05	0.54	0.31	0.10	0.04
19	SWIRE3_J104948.86+573458.2	10.89	0.37	0.07	0.37	0.51	0.06	0.06
11	SWIRE3_J103515.83+573337.4	10.87 ± 0.12	0.10	-0.02	0.34	0.29	0.24	0.12
21	SWIRE3_J105041.96+570706.7	10.76	0.35	0.06	0.37	0.51	0.06	0.06
29	SWIRE3_J105207.16+570745.5	10.73	-0.12	0.01	0.72	0.25	0.02	0.00
37	SWIRE3_J105318.94+572140.7	10.70	-0.16	0.05	0.72	0.25	0.02	0.00
2	SWIRE2_24_J103249.4+573707	10.67	0.04	0.03	0.54	0.31	0.10	0.04
34	SWIRE3_J105301.36+570543.1	10.64	-0.05	0.03	0.54	0.31	0.10	0.04
7	SWIRE3_J103327.90+574534.4	10.60	-0.05	0.02	0.54	0.31	0.10	0.04
14	SWIRE3_J103539.24+574243.9	10.58	0.16	0.04	0.54	0.31	0.10	0.04
27	SWIRE3_J105150.50+573905.7	10.56	0.15	0.04	0.54	0.31	0.10	0.04
18	SWIRE3_J103653.50+575442.5	10.46	-0.19	0.03	0.72	0.25	0.02	0.00
40	SWIRE3_J105432.31+570932.4	10.44	0.20	0.03	0.54	0.31	0.10	0.04
33	SWIRE3_J105256.85+570825.6	10.40	0.32	0.05	0.22	0.47	0.19	0.12
26	SWIRE3_J105143.75+572936.9	10.18	0.27	0.05	0.37	0.51	0.06	0.06
3	SWIRE3_J103253.94+580633.0	10.17	-0.27	0.02	0.72	0.25	0.02	0.00
30	SWIRE3_J105225.75+570153.6	10.16	-0.44	0.01	0.90	0.03	0.02	0.05
24	SWIRE3_J105100.42+574114.9	10.12	-0.14	0.01	0.72	0.25	0.02	0.00
38	SWIRE3_J105320.92+571433.2	10.03	0.45	0.02	0.22	0.47	0.19	0.12
20	SWIRE3_J104956.06+571440.4	$9.98^{+0.37}_{-0.46}$	0.16	0.03	0.54	0.31	0.10	0.04
17	SWIRE3_J103606.48+574702.4	9.95	-0.30	0.03	0.72	0.25	0.02	0.00
22	SWIRE3_J105052.41+573506.9	9.64	0.07	0.04	0.54	0.31	0.10	0.04
4	SWIRE2_24_J103258.0+573105	9.55	0.29	0.03	0.22	0.47	0.19	0.12
39	SWIRE3_J105349.60+570708.1	8.81	0.42	0.03	0.22	0.47	0.19	0.12

Note. — Sources in the LHNW and LHEX fields listed in order of decreasing L_{IR} . Columns give RA ordered counter number, source ID, infrared luminosity (8-1000 μm) in units of $\log(L_{\odot})$, corrected P1 color, corrected P2 color, Star-Forming probability, Composite probability, AGN probability, and No Emission-Line probability calculated by comparing P1 and P2 colors with those of the IRAS sample (see Appendix).

*Sources J103538.8+573546 and J103341.28+580221.4 suffer from contamination due to partially overlapping foreground galaxies, which prohibits determining accurate P1,P2 colors. Source J105151.64+570935.7 is spectroscopically classified as a Seyfert and is suspected to harbor a QSO, thus the use of P1,P2 color to determine spectral type is inappropriate.